Interactions between ultra-high-energy particles and protogalactic environments

Ellis R. Owen,[1,2]★ Idunn B. Jacobsen,[1] Kinwah Wu[1] and Pooja Surajbali[3,4]

[1]*Mullard Space Science Laboratory, University College London, Holmbury St. Mary, Dorking, Surrey, RH5 6NT, UK*
[2]*Institute of Astronomy, Department of Physics, National Tsing Hua University, Hsinchu, Taiwan (ROC)*
[3]*Department of Physics & Astronomy, University College London, Gower Street, London, WC1E 6BT, UK*
[4]*Max-Planck-Institut für Kernphysik, Saupfercheckweg 1, Heidelberg D-69117, Germany*

ABSTRACT

We investigate the interactions of energetic hadronic particles (cosmic ray protons) with photons and baryons in protogalactic environments, where the target photons are supplied by the first generations of stars to form in the galaxy and the cosmological microwave background, while the target baryons are the interstellar and circumgalactic medium. We show that pair-production and photo-pion processes are the dominant interactions at particle energies above 10^{19} eV, while proton-proton (pp) interaction pion-production dominates at the lower energies in line with expectations from, for example γ-ray observations of star-forming galaxies and dense regions of our own galaxy's interstellar medium. We calculate the path lengths for the interaction channels and determine the corresponding rates of energy deposition. We have found that protogalactic magnetic fields and their evolution can significantly affect the energy transport and energy deposition processes of cosmic rays. Within a Myr after the onset of star-formation the magnetic field in a protogalaxy could attain a strength sufficient to confine all but the highest energy particles within the galaxy. This enhances the cosmic ray-driven self-heating of the protogalaxy to a rate of around 10^{-24} erg cm^{-3} s^{-1} for a galaxy with strong star-forming activity that yields one core collapse supernova event per year. This heating power exceeds even that due to radiative emission from the protogalaxy's stellar populations. However, in a short window before the protogalaxy is fully magnetized, energetic particles could stream across the galaxy freely, delivering energy into the circumgalactic and intergalactic medium.

Key words: cosmic rays – ISM: evolution – ISM: magnetic fields – galaxies: clusters: general – galaxies: high-redshift.

1 INTRODUCTION

High-energy hadronic particles heat the media along their propagation paths by collisional ionization and hadronic interactions, with such action of cosmic rays (CRs) having been observed close-by in the Earth's atmosphere (see e.g. Ginzburg 1996; Kotera & Olinto 2011, for reviews). A substantial fraction of the energetic CRs detected on the Earth are protons (Abbasi et al. 2010), and their origins are likely to be extragalactic. The interactions of CRs in astrophysical environments have also been discussed in the literature in various contexts (e.g. Greisen 1966; Zatsepin & Kuz'min 1966; McCray & Buff 1972; Nath & Biermann 1993; Valdés, Evoli & Ferrara 2010). While research into CRs in solar-terrestrial settings has progressed a long way since their discovery, the role of

ultra-high-energy (UHE) CR particles in galaxies and larger structures is less well understood – even in systems where these energetic particles are evidently abundant, such as in star-forming galaxies (see e.g. Karlsson 2008; Lacki et al. 2011; Lacki & Thompson 2012; Wang & Fields 2014) and galaxy clusters (see e.g. Brunetti & Jones 2014). It has been argued that CRs can regulate star formation in a galaxy (see Pfrommer et al. 2007; Chen, Bryan & Salem 2016) and that their heating effect could drive large-scale galactic wind outflows (see Socrates, Davis & Ramirez-Ruiz 2008; Weiner et al. 2009). Not only do UHECRs alter the dynamical and thermal properties of their galaxy of origin, they can also transport energy from their host to the surrounding intergalactic medium. While CR heating and ionization operate in nearby galaxies, conditions in the very distant Universe imply that CR processes are expected to be even more important when young galaxies were spawning their first generation of stars and luminous quasars first emerged. The effects of CRs in the high-redshift Universe are now beginning to be

★ E-mail: ellis.owen.12@ucl.ac.uk

recognized (see Giammanco & Beckman 2005; Stecker, Malkan & Scully 2006; Valdés et al. 2010; Bartos & Marka 2015; Sazonov & Sunyaev 2015; Walker 2016; Leite et al. 2017).

CRs are products of violent astrophysical events, e.g. supernova (SN) explosions, gamma-ray bursts, large-scale shocks in colliding galaxies and galaxy clusters, and extreme environments in compact objects, e.g. fast spinning neutron stars and accreting black holes (see Berezinsky, Gazizov & Grigorieva 2006; Dar & de Rújula 2008; Kotera & Olinto 2011). As strong star-formation activity gives rise to frequent SN events, galaxies with active, ongoing star formation are naturally strong CR sources. In these galaxies, the stars and their remnants supply the seed particles, and the shocks generated by the SN explosions and other violent events provide the needed mechanisms for accelerating the particles to very high energies, e.g. through Fermi acceleration processes (Fermi 1949).

Atomic matter can be ionized and excited by keV CR protons and this can heat the interstellar and intergalactic medium (see e.g. Nath & Biermann 1993; Sazonov & Sunyaev 2015). However, compared to their higher-energy counterparts, a galactic population of sub-GeV CRs only contains sufficient energy to drive a relatively small heating effect, even if all of their energy were to be deposited within a reasonable time-scale. This is because less than 1 per cent of the total CR energy is harboured in these lower energy particles (see e.g. Benhabiles-Mezhoud et al. 2013). Higher-energy CRs (i.e. those with energy $\gtrsim 1$ GeV) are much less engaged with atomic interactions. If ionization and atomic excitation were the only means of energy exchange, a 0.5 GeV CR-proton would lose less than 2.5 per cent of its initial energy on a Hubble time-scale as it propagates across a cosmological baryonic density field, even when the density is maintained as that at redshift $z = 20$ (see Sazonov & Sunyaev 2015). However, the distance a CR particle above GeV energies can propagate in an interstellar or intergalactic medium is instead determined by hadronic processes. The Gresisen–Zatsepin–Kuzmin cut-off (Greisen 1966; Zatsepin & Kuz'min 1966) is an example of such, where CRs are suppressed by their hadronic interactions with cosmic microwave background (CMB) photons.

The impact of CRs depends on their interaction channels with the matter and radiation fields (microscopic particle physics) and also on the properties of the media through which the CRs propagate (microscopic astrophysics). How CRs affect the interior and exterior environments of their host galaxy is determined by the ability of the galaxy to act as a CR calorimeter (accounting for the galactic density profile and substructure), its regulation of CR diffusion, the properties of its global outflows and the entrapment of charged particles by its magnetic field (see Thompson, Quataert & Waxman 2007; Tueros, del Valle & Romero 2014; Kobzar et al. 2016).

In this work we investigate the effects of energetic CR particles in high redshift protogalactic environments. We adopt a phenomenological approach that sufficiently captures the essence of the relevant physics and astrophysics. Complexities such as the CR compositions at different stages of galactic evolution or the exact production and acceleration mechanisms of various types of primary particles in specific galactic components are finer details that will be left to future follow-up studies. Our focus is on the interactions of the particles with the radiation and baryon density fields and how efficiently energy is deposited along the particle propagations in the interstellar and intergalactic media.

We organize the paper as follows. In Section 2, we introduce the hadronic processes relevant to CR heating of the astrophysical media. In Section 3, we specify the protogalactic model that provides the baryonic density profile, radiation properties, and magnetic fields through which the propagations and interactions of the CRs are calculated. In Section 4, we show the results of our calculations, and we discuss their consequences and astrophysical implications in Section 5. We particularly focus on those implications concerning propagation distances and energy deposition rates of the CRs and particle confinement in response to the evolution of the magnetic field of the host galaxy.

For the remainder of this discussion, we refer to the UHECR protons as CRs, unless stated otherwise. For clarity we may also refer specifically to CR protons and CR electrons to differentiate between the two where appropriate, but when unspecified we refer to the proton component of CRs. We do not consider primary CR electrons in detail as their energy loss rate is considerably more rapid compared to the CR protons. Therefore, their energy is deposited much more locally to their source and is less important in the global model we present here.

2 PARTICLE INTERACTIONS

Photo-pion (pγ) production, Bethe–Heitler pair production, and pp pion-production interactions are the relevant processes governing the interaction of hadronic CRs with radiation and matter in astrophysical environments. These processes produce a variety of hadrons, including charged and neutral pions, neutrons, and protons (see Pollack & Fazio 1963; Gould & Burbidge 1965; Stecker, Tsuruta & Fazio 1968; Mücke et al. 1999; Berezinsky et al. 2006; Dermer & Menon 2009). The secondary particles produced will continue to undergo hadronic interactions, resulting in particle cascades. Neutral pions predominantly decay into two photons through an electromagnetic process,

$$\pi^0 \rightarrow 2\gamma \tag{1}$$

with a branching ratio of 98.8 per cent (Patrignani et al. 2016) and on a time-scale of 8.5×10^{-17} s. Charged pions predominantly produce leptons and neutrinos via a weak interaction,

$$\pi^+ \rightarrow \mu^+ \nu_\mu \rightarrow e^+ \nu_e \bar{\nu}_\mu \nu_\mu$$
$$\pi^- \rightarrow \mu^- \bar{\nu}_\mu \rightarrow e^- \bar{\nu}_e \nu_\mu \bar{\nu}_\mu \tag{2}$$

with a branching ratio of 99.9 per cent (Patrignani et al. 2016) but on a longer time-scale of roughly 2.6×10^{-8} s.

As the majority of the CR particles observed on the Earth are protons (see Abbasi et al. 2010), we boldly assume that the particles and the baryons in the protogalactic environment are protons. The energy of the incident particles is $E_p = \gamma_p m_p c^2$, where γ_p is the Lorentz factor. When normalized to the electron mass this is $\varepsilon_p = \gamma_p (m_p/m_e)$. The target baryons may be assumed to be at rest without losing generality with normalized energy $\varepsilon = m_p/m_e$. Correspondingly, the normalized energy of a target photon of frequency ν is given by $\varepsilon = h\nu/m_e c^2$. In photo-pion production calculations, it is useful to define an invariant normalized energy, $\varepsilon_r = \gamma_p (1 - \beta_p \mu)\varepsilon$, where μ is the cosine of the angle between the momentum vectors of the incident proton and the photon and β_p is the proton velocity normalized to the speed of light. These variables will be used hereafter.

The length scale over which a proton with energy E_p would lose its energy through an interaction is

$$r_{int} = \left\{ \frac{d \ln E_p}{ds} \right\}^{-1} = \left\{ \frac{d \ln \epsilon_p}{ds} \right\}^{-1} \tag{3}$$

where ds is the differential path length element (see Blumenthal 1970). The energy loss length-scale may also be expressed in terms of the interaction time-scale t_{int}, i.e.

$$r_{int} \approx c\beta_p t_{int} . \tag{4}$$

We adopt this expression in the calculations of the effective path length and the energy deposition rate of CRs in our protogalactic model environments.

In our calculations, we restrict the particle energies to between 10^9 and 10^{20} eV. These energies are sufficient to account for the relevant hadronic processes in protogalactic environments. When modelling the CR production by SN events in protogalaxies, we further restrict the maximum particle energy to 10^{15} eV. This is a more realistic bound on the energies that could be attained by CRs accelerated in an SN remnant (e.g. Bell 1978; Kotera & Olinto 2011; Bell 2013; Bell et al. 2013; Schure & Bell 2013; Schure & Bell 2013), with higher energy particles likely to have an origin outside a typical protogalaxy (e.g. Hillas 1984; Becker 2008; Kotera & Olinto 2011; Blasi 2014). Below 10^9 eV (i.e. 1 GeV), CRs are not thought to contain sufficient energy to drive a strong heating effect as they cannot undergo hadronic interactions below the GeV-level threshold energy. Although the validity of this proposition is not strictly guaranteed, taking an alternative approach does not imply more correct physics. We lack concrete knowledge of the properties of CRs outside our own solar system, so those in the very furthest corners of the Universe are even less well known. We therefore omit unnecessary complications arising from the spatial variations and time evolution of cosmological CR spectra, and adopt these working assumptions.

2.1 Photo-pion production

2.1.1 Interaction channel and cross-section

Photo-pion production arises when incident protons collide with the photons of a radiation field. The dominant interactions in photo-pion production are (i) resonant single-pion production, (ii) direct single-pion production, and (iii) multiple-pion production (Mücke et al. 1999). Other processes (e.g. diffractive scattering), though present, are less significant. The total cross-section of photo-pion production is therefore the sum of the cross-sections of these three main interactions.

Resonant single-pion production occurs through the production of Δ^+ particles that decay through two major channels,

$$p\gamma \to \Delta^+ \to \begin{cases} p\pi^0 \to p2\gamma \\ n\pi^+ \to n\mu^+ \nu_\mu \\ \qquad\quad \hookrightarrow e^+ \nu_e \bar{\nu}_\mu \end{cases} \tag{5}$$

(see Berezinsky & Gazizov 1993), where charged and neutral pions are produced. The branching ratios for the $\Delta^+ \to \pi^0$ and $\Delta^+ \to \pi^+$ channels are 2/3 and 1/3, respectively. Direct pion production is less efficient, and its rate is roughly 1/3 of that of the resonant single-pion production at $\varepsilon_r \approx 500$. While single-pion production dominates at energies ε_r below ≈ 3500, multipion production occurs at higher energies (see Mücke et al. 1999).

Neutrons have a half-life of about 880 s (Nakamura 2010). If not colliding with other particles, the neutrons produced in the resonant single-pion process will undergo β^--decay,

$$n \to pe^- \bar{\nu}_e . \tag{6}$$

However, they may instead interact with the radiation field, which will lead to further p and π^- production,

$$n\gamma \to \Delta^0 \to \begin{cases} p\pi^- \\ n\pi^0 \end{cases} \tag{7}$$

with branching ratios $BR(\Delta^0 \to \pi^-) = 1/3$ and $BR(\Delta^0 \to \pi^0) = 2/3$ (Hümmer et al. 2010).

These branching ratios appear to imply that there would be more neutral pions than charged pions in single-pion production processes. However, when taking the additional charged pions produced in the residual interactions into account (which include $p\gamma \to \Delta^{++}\pi^-$, $\Delta^0\pi^+$), each type of pion is found to be produced in roughly equal numbers (see Dermer & Menon 2009).

Experimental data (Baldini et al. 1987) indicate that the total cross-section of the photo-pion interaction may be divided into three energy regions of average cross-sections

$$\sigma_{\gamma\pi}(\epsilon_r) \approx \begin{cases} 340\mu b & [\epsilon_{th} \leq \epsilon_r < 980] \\ 240\mu b & [980 \leq \epsilon_r < 3500] \\ 120\mu b & [3500 \leq \epsilon_r] \end{cases} \tag{8}$$

(cf. the approximated two-step function used in Dermer & Menon 2009), where $\varepsilon_{th}(\approx 390)$ is the threshold energy for the pion production process. The lower-energy incident protons will lose approximately 20 per cent of their energy in the resonant single-pion production process, with similar rates for the neutral and charged pion channels. The higher-energy incident protons will lose approximately 60 per cent of their energy in the multiple-pion production process (Dermer & Menon 2009). The effective inelastic cross-section is $\hat{\sigma}_{\gamma\pi} \equiv \sigma_{\gamma\pi}(\epsilon_r)K_{\gamma\pi}(\epsilon_r)$, with the inelasticity coefficient

$$K_{\gamma\pi}(\epsilon_r) \approx \begin{cases} 0.2 & [\epsilon_{th} \leq \epsilon_r < 3500] \\ 0.6 & [3500 \leq \epsilon_r] \end{cases} . \tag{9}$$

This yields

$$\hat{\sigma}_{\gamma\pi} \approx \begin{cases} 68\mu b & [\epsilon_{th} \leq \epsilon_r < 980] \\ 48\mu b & [980 \leq \epsilon_r < 3500] \\ 72\mu b & [3500 \leq \epsilon_r] \end{cases} . \tag{10}$$

If we ignore the small variations in $\hat{\sigma}_{\gamma\pi}$ over ε_r, the effective cross-section may be expressed as $\hat{\sigma}_{\gamma\pi} \approx \hat{\sigma}_{\gamma\pi}^* \mathcal{H}(\varepsilon_r - \epsilon_{th})$, where $\mathcal{H}(...)$ is the Heaviside step function. In our calculations we adopt $\hat{\sigma}_{\gamma\pi}^* = 70\mu b$ and $\varepsilon_{th} = 390$, which are the same as the values suggested by Dermer & Menon (2009) (see also Atoyan & Dermer 2003).

2.1.2 Energy loss

In a protogalactic environment, the target photons for photo-pion production are expected to be supplied by the stellar sources and the CMB. For the CMB, the radiation is locally isotropic and, in both cases, the spectrum is well modelled by a blackbody. The photon number density is given by a *Planck* function:

$$n(\epsilon) = \frac{8\pi}{\lambda_C^3} \frac{\epsilon^2}{e^{\epsilon m_e c^2/k_B T} - 1} \tag{11}$$

where $\lambda_C = h/m_e c$ is the electron Compton wavelength and T is the effective temperature of the source. In an isotropic radiative field with a blackbody spectrum, the time-scale for the photo-pion interaction is

$$t_{\gamma\pi}(\gamma_p) = \frac{2\gamma_p^2 \lambda_C^3}{8\pi c} \left\{ \int_0^\infty \frac{d\epsilon}{e^{\epsilon m_e c^2/k_B T} - 1} \int_0^{2\gamma_p \epsilon} d\epsilon_r \epsilon_r \hat{\sigma}_{\gamma\pi} \right\}^{-1} \tag{12}$$

in the high-energy limit, i.e. $\beta_p \rightarrow 1$ [1] (Dermer & Menon 2009). Thus, the energy of the incident proton is deposited over a path length $r_{\gamma\pi} = c\beta_p t_{\gamma\pi}(\gamma_p)$. With $\beta_p \approx 1$ and approximating the cross-section as $\hat{\sigma}_{\gamma\pi} \approx \hat{\sigma}^*_{\gamma\pi} \mathcal{H}(\epsilon_r - \epsilon_{th})$, we may evaluate the latter integral in equation 12, and by imposing the requirement that $2\gamma_p \epsilon \geq \epsilon_{th}$ we obtain

$$r_{\gamma\pi} \approx \frac{\lambda_C^3}{8\pi\hat{\sigma}^*_{\gamma\pi}} \left(\frac{m_e c^2}{k_B T} \right)^3 \mathcal{J}^{-1} \tag{13}$$

where

$$\mathcal{J} = \int_\eta^\infty d\zeta \, \frac{\zeta^2 - \eta^2}{e^\zeta - 1} = 2\sum_{k=1}^\infty \left(\frac{\eta}{k^2} + \frac{1}{k^3} \right) e^{-k\eta} \tag{14}$$

and $\eta = \epsilon_{th} m_e c^2 / 2\gamma_p k_B T$.

2.2 Photo-pair production

2.2.1 Interaction channel and cross-section

Leptons can be produced in photo-hadronic interactions through the Bethe–Heitler process (Bethe & Heitler 1934)

$$A\gamma \rightarrow A' l^+ l^- \tag{15}$$

where A and A' are nucleons, and l^+ and l^- are positively and negatively charged leptons, respectively. Photo-electron pair production

$$p\gamma \rightarrow p e^+ e^- \tag{16}$$

is a Bethe–Heitler process and is the key contribution to photo-pair CR-energy losses (see e.g. Blumenthal 1970; Klein 2006) over the range of energies of interest in this work. Stepney & Guilbert (1983) considered an analytic fit to the cross-section for photo-electron pair production and obtained

$$\hat{\sigma}_{\gamma e}(\epsilon_r) \approx \left\{ \frac{7}{6\pi}\alpha_f \left(\psi - \frac{109}{42} \right) + \left[473.65 + 241.26\psi \right. \right.$$
$$\left. \left. + 81.151\psi^2 + 5.3814\psi^3 \right] \left(\frac{10^{-5}}{\epsilon_r} \right) \right\} \sigma_T \tag{17}$$

(see also Jost, Luttinger & Slotnick 1950; Bethe & Maximon 1954; Blumenthal 1970), where α_f is the fine structure constant, σ_T is the Thomson cross-section, and $\psi = \ln 2\epsilon_r$. For the parameter regime relevant to this study, $\epsilon_r \gtrsim 60$, and the expression for the cross-section above may be approximated as

$$\hat{\sigma}_{\gamma e}(\epsilon_r) \approx \left\{ \frac{7}{6\pi}\alpha_f \ln \left[\frac{\epsilon_r}{k_{\gamma e}} \right] \right\} \sigma_T \tag{18}$$

with $k_{\gamma e}$ taking a value of ≈ 6.7. Without losing generality, we fix $k_{\gamma e} = 6.7$ in our calculations, which we find to be appropriate for the energy range of interest. Note that the same expression for the cross-section (equation 18) was given in Dermer & Menon (2009), but $k_{\gamma e} = 2$ (for $\epsilon_r \gtrsim 40$) was considered instead.

2.2.2 Energy loss

Assuming that the electron-positron pair produced in the photo-pair production process is formed at rest in the zero-momentum frame of the interaction (Dermer & Schlickeiser 1991) and that the invariant

[1] Note that while this result is valid for the CMB, stellar emission radiates from discrete points and requires a correction factor (see Section 3).

energy of the interaction is much larger than that of the target photon field such that the interaction energy is specified by the CR energy, the time-scale for interactions with a blackbody radiation field is

$$t_{\gamma e} \approx \frac{m_p}{m_e} \frac{\gamma_p^2}{c} \left\{ \int_{\gamma_p^{-1}}^\infty d\epsilon \, \frac{n_{ph}(\epsilon)}{\epsilon^2} \int_2^{2\gamma_p\epsilon} d\epsilon_r \frac{\epsilon_r \hat{\sigma}_{\gamma e}(\epsilon_r)}{\sqrt{1 + 2\epsilon_r}} \right\}^{-1} \tag{19}$$

(see Protheroe & Johnson 1996; Dermer & Menon 2009), which implies an interaction path length of

$$r_{\gamma e}(\gamma_p) \approx \frac{9}{112} \frac{m_p \lambda_C^3 \gamma_p^3 b^{5/3}}{m_e \alpha_f \sigma_T \mathcal{F}_{\gamma e}} \text{ Gpc} \tag{20}$$

where $b = m_e c^2 / \gamma_p k_B T$ and

$$\mathcal{F}_{\gamma e} = \mathcal{C}(b) + \mathcal{D}(b) \ln \left[\frac{1}{0.974 b k_{\gamma e}} \right] + \left(0.382 b k_{\gamma e} \right)^{3/2} \mathcal{E}(b) . \tag{21}$$

The functions $\mathcal{C}(b)$, $\mathcal{D}(b)$, and $\mathcal{E}(b)$ result from standard integrals, with $\mathcal{C}(b) = 0.74$ and $\mathcal{D}(b) = \Gamma(5/2)\zeta(5/2)$ when $b \ll 1$, $\mathcal{C}(b) = b^{3/2} \ln(b)e^{-b}$ and $\mathcal{D}(b) = b^{3/2}e^{-b}$ when $b \gg 1$, and $\mathcal{E}(b) = -\ln[1 - e^{-b}]$ for all values of b (Dermer & Menon 2009). Note that equation (20) requires an additional factor in the case of a diluted radiation field (see Section 3).

2.3 pp pion production

2.3.1 Interaction channel and cross-section

Like photo-pion production, pp pion production also produces charged and neutral pions, which subsequently undergo decays to deposit energy into their ambient medium. The interaction leads to the following dominant pion production channels

$$p + p \rightarrow \begin{cases} p\Delta^+ \rightarrow \begin{cases} pp\pi^0\xi_0(\pi^0)\xi_\pm(\pi^+\pi^-) \\ pp\pi^+\pi^-\xi_0(\pi^0)\xi_\pm(\pi^+\pi^-) \\ pn\pi^+\xi_0(\pi^0)\xi_\pm(\pi^+\pi^-) \end{cases} \\ n\Delta^{++} \rightarrow \begin{cases} np\pi^+\xi_0(\pi^0)\xi_\pm(\pi^+\pi^-) \\ nn2\pi^+\xi_0(\pi^0)\xi_\pm(\pi^+\pi^-) \end{cases} \end{cases} \tag{22}$$

where ξ_0 and $\xi_\pm$ are the multiplicities for neutral and charged pions, respectively, and the Δ^+ and Δ^{++} baryons are the resonances (see Almeida et al. 1968; Skorodko et al. 2008). The inelasticity, i.e. fraction of hadronic energy lost to pion production is around 0.6 (similar to the photo-pion interaction). The rest of the energy mainly goes into secondary hadronic particles which can interact further along their propagations. Appendix B demonstrates that almost 100 per cent of the original energy is transferred to pion production within just a small number of interactions.

The total inelastic cross-section is well described by the analytic parametrization

$$\hat{\sigma}_{p\pi} = \left(30.7 - 0.96\ln(\chi) + 0.18(\ln\chi)^2 \right) \left(1 - \chi^{-1.9} \right)^3 \text{ mb} \tag{23}$$

(Kafexhiu et al. 2014), where $\chi = E_p / E_p^{th}$, and the threshold energy $E_p^{th} = (2m_{\pi^0} + m_{\pi^0}^2 / 2m_p)c^2 \approx 0.28$GeV is the proton energy required for the production of a neutral pion through

$$pp \rightarrow pp\pi^0 . \tag{24}$$

The branching ratios for the production of each pion species across all relevant channels can be estimated by considering their respective production cross-sections. We find that the parametrizations

given by Blattnig et al. (2000) offer a reasonable fit to the data, accounting for single-pion and multipion production channels.[2] This gives branching ratios for the production of $\{\pi^+, \pi^-, \pi^0\}$ as {0.6, 0.1, 0.3} at 1 GeV while, at higher energies, this levels out to {0.3, 0.4, 0.3}. This gives the total fraction of energy passed to neutral pions as around 0.3, while that going to charged pion production is around 0.7, of which 0.1 is lost to neutrinos (Dermer & Menon 2009). The charged pions can further decay to electrons and further neutrinos by the weak interaction outlined in process 2. The neutrinos in this decay adopt around 75 per cent of the pion energy, while the remainder is passed to the electron and positron products and shared approximately equally between them according to their production multiplicity (see e.g. Aharonian & Atoyan 2000; Loeb & Waxman 2006; Lacki & Thompson 2012; Lacki & Beck 2013). Overall, this gives an inelasticity in the pp interaction of around 0.15 for the production of secondary electrons and positrons.[3]

2.3.2 Energy loss

The effective path length for CRs undergoing pp interactions is more straightforward than in previous cases. Before the target field was comprised of photons, so a full relativistic treatment was necessary. Here, the target field is comprised of low-energy, non-relativistic baryons that can be approximated as an ensemble of stationary particles. In this regime, the interaction path length is comparable to the classical definition of the mean free path

$$r_{p\pi} = \frac{1}{\hat{\sigma}_{p\pi} n_p}, \tag{25}$$

where n_p is the baryon number density in the target field and $r_{p\pi}$ is the effective CR proton path length.

3 THE PROTOGALACTIC ENVIRONMENT

Some protogalaxies exhibit strong, ongoing star-forming activity (see e.g. Di Fazio, Occhionero & Vagnetti 1979; Solomon & Van-den Bout 2005; Pudritz & Fich 2012; Ouchi et al. 2013; Knudsen et al. 2016), which inevitably results in a high rate of SN events. SN explosions generate shocks, providing a viable mechanism for particle acceleration (e.g. Berezhko & Ellison 1999; Allard, Parizot & Olinto 2007; Blasi 2011; Bell et al. 2013; Schure & Bell 2013). Frequent SN events inject substantial energy into their host galaxies that can power a strong galactic wind outflow (cf. the nearby starburst galaxy M82). Shocks in such a galactic wind, like the SN-generated shocks, can also serve as particle acceleration sites.

Because of the larger spatial scales of galactic winds, CRs may achieve even higher energies than in SN shocks if the magnetic field strengths in the two cases are similar (see Hillas 1984). Moreover, star-forming activity and associated SN events would give rise to a population of young compact objects, which are potential particle accelerators (see e.g. Dar & de Rújula 2008; Kotera & Olinto 2011). Protogalaxies are therefore conducive environments

for particle acceleration, and the CRs they produce would in turn affect the thermal properties of the ISM within the galaxy and local intergalactic medium (IGM).

Here we adopt a generic model in which a protogalaxy is a parametric mean to specify the baryon field, radiation field and magnetic field at a redshift of $z = 7$. The complicated dynamical and internal star-forming processes of the galaxies are ignored, and left to future work. Moreover, as an initial study, we assume that the CRs produced by local SN activity (assumed to be protons) interact with only these three fields, and the energy losses of the CRs are determined by their corresponding interaction processes.

3.1 Density field

We model the (baryon) density field as an overdensity on the background medium using the profile

$$n_b(r) = \frac{n_{b,0}}{(1 + \xi_c)(1 + \xi_h)} \tag{26}$$

(Dehnen 1993), where $\xi_c = (r/r_c)^2$ and $\xi_h = (r/r_h)^2$ for r_c and r_h as the galaxy profile core and halo radius, respectively, as introduced in Dehnen (1993) and Tremaine et al. (1994). This model is chosen for analytical tractability while still being a reasonable description of the gas profile in an elliptical galaxy for which the mass $M(< r)$ does not diverge with increasing radius, r. The core and halo radius are specified for each galaxy model. The values used for the parameters in this case are $r_c = 1$ kpc and $r_h = 2$ kpc. The normalization n_0 of the profile is $10 \, \text{cm}^{-3}$, being a characteristic density of the protogalactic interstellar medium (ISM).

For the purposes of this study, the baryon profile is superposed onto a background density of $n_p = 10^{-3} \, \text{cm}^{-3}$. This fiducial value is taken as an example value to represent one possible intracluster medium environment in which such a protogalaxy may be found. While a range of values either side of this would be reasonable for the various cluster environments and neighbourhoods in which such a protogalaxy may be found, we find the exact choice (if reasonable) bears little influence on the results of this study and focus of the discussion here.

3.2 Radiation field

The radiation field plays two roles in this model. First, as a target for the CRs in photo-pair and photo-pion interactions and, secondly, as a source of stellar radiation to drive a (conventional) heating effect with which the CR heating can be compared. In the first case, we must estimate the number density of target photons for CR interactions while, in the second case, the radiative stellar and X-ray flux are required.

3.2.1 Radiation as a CR target

The spatial profile of the radiation field is governed by two factors: (1) the distribution of sources within the model protogalaxy and (2) the geometric spreading of photons as they radiate from their sources. In the case of a point source, the latter of these is described simply by the inverse square law, but for instances where the source is described more correctly by a distribution, a more general result is required.

We assume that the stellar distribution in the galaxy follows the underlying Dehnen (1993) density profile introduced in Section 3.2, up to cut-off of $R = 10$ kpc above which we do not place any stars. It should be noted that the vast majority of the stellar contribution

---

[2] We find that there is a minor discrepancy between data at lower energies below 50 GeV and the Blattnig et al. (2000) parametrizations, but the difference is sufficiently small for our purposes.

[3] We acknowledge that our estimated inelasticity value is marginally lower than the 0.17 value quoted in Aharonian & Atoyan (2000), and implied in Lacki & Beck (2013); Loeb & Waxman (2006). We believe this is due to our additional inclusion of the 10 per cent losses to neutrinos in the charged pion production process.

is within $r_c = 1$ kpc (see e.g. Mosleh et al. 2012; Ono et al. 2013; Whalen et al. 2013) and this high cut-off is intended to avoid a sharp unphysical edge to the galaxy.

Assuming that the radiative emission of the galaxy is dominated by that from stars, and that each star may be modelled as a black-body of temperature $T_* = 30\,000$ K (i.e. type O/B), we can model the radiation field around a single source starting with the stellar luminosity, given by the Stefan–Boltzmann relation as

$$L_* = 4\pi R_*^2 \sigma T_*^4 \tag{27}$$

where R_* is the stellar radius. The energy density near a source is then

$$U_* = \frac{L_*}{4\pi r^2 c} . \tag{28}$$

The photon number density of the field is estimated by dividing the energy density by the modal photon energy. This is estimated as $E_{ph} = 2.82 k_B T_* \approx 3 k_B T_*$, being roughly the peak of the spectrum of the radiation field, hence

$$n_{ph} \approx \frac{U_*}{3 k_B T_*} . \tag{29}$$

The generalization from a point source to a distribution is derived in Appendix A, with the result given by equation (A8). This gives the stellar photon number density profile as

$$n_{ph}(r) \approx \frac{L_* \cdot N \cdot \omega(r)}{4\pi r_{gal}^2 c \, k_B T_* D_N} \tag{30}$$

where $\omega(r)$ is further introduced as a weighting (in this case the normalized density profile), and with $D_N = 1 + N^{-1/3} + N^{-2/3}$ for N as the number of stars. We use $N = 10^6$, a size of stellar population that provides a stellar luminosity consistent with a galaxy of SN rate $\mathcal{R}_{SN} \approx 0.1\,\mathrm{yr}^{-1}$, or star-formation rate $\mathcal{R}_{SF} \approx 16 \mathrm{M}_\odot \mathrm{yr}^{-1}$, in line with relations determined from, e.g. Starburst99 simulations (see e.g. Hirashita, Buat & Inoue 2003; Leitherer et al. 1999, for details).

We may estimate the relative importance of losses due to proton–photon interactions with this radiation field by considering the effective interaction path lengths introduced in Section 2. These do not account for the spreading of the radiation field due to the spatial distribution of the sources within the protogalaxy. Therefore, a scaling factor of n_A/n_{ph} is applied to $r_{\gamma\pi}$ and $r_{\gamma e}$ (equations 13 and 20, respectively), where n_A is the photon number density at the surface of the radiation source (essentially being the integrated blackbody spectrum, $n_A = 8\pi\Theta^3\Gamma(3)\zeta(3)/\lambda_C^3$ and n_{ph} is the estimated photon number density within the galaxy, using equation (30) above. Θ is defined by the temperature of the radiation source, in this case the stellar temperature, $T_* = 30,000$ K.

Additionally, the CMB permeates the protogalaxy. This is modelled as a spatially uniform blackbody of characteristic temperature determined by the redshift, as per equation (11), where $\Theta(z) = k_B T(z)/m_e c^2$ and $T(z) = T_0(1 + z)$ is the redshift-dependent temperature of the radiation field with $T_0 = 2.73$ K as the present CMB temperature (Planck Collaboration XIII 2016b). The resulting target radiation field relevant to the CR interactions is then the sum of both the stellar emission and the CMB.

We present in Fig. 1 the CR energy-loss components due to each of the interactions outlined in Section 2 in terms of their energy-dependent effective path lengths. For a protogalaxy such as this, it is apparent that the relative importance of the stellar photons is negligible, given that the associated path lengths (lines 3 and 4, respectively) are longer than those due to CMB interactions (red lines 5, 6, and 7). In turn, these losses are negligible compared
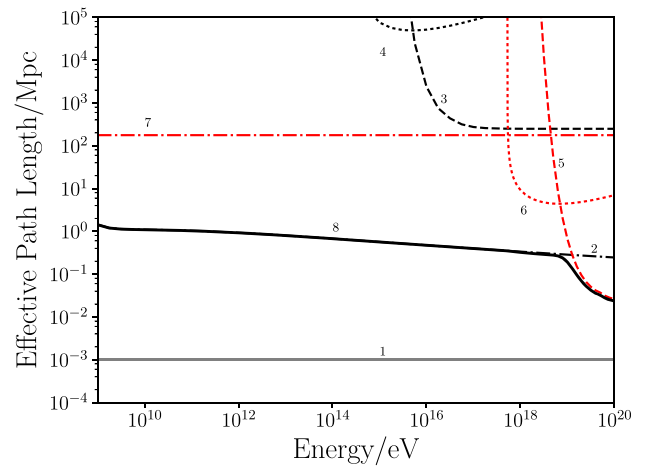
Figure 1. Plot to show the CR proton losses in terms of effective interaction path lengths. This results from a protogalaxy model with $n_p = 10 \mathrm{cm}^{-3}$ and $N_* = 10^6$, no galactic magnetic field and an underlying CMB radiation field at a redshift of $z = 7$. The loss components due to the CMB are shown in red whereas those due to the foreground galaxy model are in black. The thick black line indicates the total effect, accounting for all energy loss contributions. The lines, as labelled, are (1) Protogalaxy Radius; (2) Pion-production (pp, p$\pi^\pm\pi^0$); (3) Galactic Radiation Photo-pion (pγ, $\pi^\pm\pi^0$); (4) Galactic Radiation Photo-pair (pγ, $e^\pm$); (5) CMB Photo-pion (pγ, $\pi^\pm\pi^0$); (6) CMB Photo-pair (pγ, $e^\pm$); (7) CMB Cosmological Expansion; and (8) Total.

to the interactions of CRs with the baryons of the galaxy (dashed black line 2) except at the very highest of energies, above 10^{19} eV, at which point the CR flux is very low and thus such interactions are unlikely to bear any important influence on any resulting total energy deposition that arises. The thick black line indicates the resultant losses calculated as the reciprocal sum of all contributions, and this is almost completely governed by the pp interactions between UHECRs and the baryon (density) field of the galaxy, not the pγ interactions (photo-pair and photo-pion). Thus, the CR propagation lengths are strongly related to the protogalactic density field, with the radiation field bearing no significant influence on the resulting losses or any CR driven heating or energy-deposition effect.[4] These loss lengths are calculated for the conditions at the centre of the model protogalaxy at $z = 7$.

3.2.2 Radiation as a source of heating

To provide a reference, we estimate the level of heating expected due to radiation from the stellar population and diffuse X-ray emission

---

[4] In addition to the loss mechanisms introduced in earlier sections, the CRs free-streaming over cosmological distances will undergo adiabatic losses due to the expanding Universe. The length-scale on which this arises is

$$r_{exp} = c \left| \frac{1}{E} \left(\frac{dE}{dt} \right)_{exp} \right|^{-1} = \frac{c}{H_0 \sqrt{\Omega_m (1 + z)^3 + \Omega_\Lambda}} \tag{31}$$

(see Gould 1975; Berezinsky & Grigor'eva 1988; Berezinsky et al. 2006), where $H_0 = (67.8 \pm 0.9)$ km s^{-1} Mpc^{-1}, $\Omega_m = 0.308 \pm 0.012$ and $\Omega_\Lambda = 0.691 \pm 0.0062$ with negligible curvature and radiation energy density contributions (Planck Collaboration XIII 2016b). These losses only become important for CRs that are not contained by the magnetic fields or interactions with their origin protogalaxy and are indicated in Fig. 1 by the dash-dotted horizontal red line (7).

throughout the protogalaxy. To do this, we employ a Monte Carlo (MC) method in which we distribute the total radiative emission across a simulated source distribution of 10 000 points. Accounting for the inverse square law and attenuation between each source point and some observation point r, the flux incident at a point r due to each source may be found. The sum of this gives the incident flux at r due to the entire source distribution. The level of heating is given by the product of the flux and the tendency of the medium at r to absorb this radiation, quantified by the absorption coefficient α – itself a product of the local number density of scatterers and the scattering cross-section of the radiation (likewise, the attenuation is determined by the integrated effect of this absorption along a photon's path). In the case of low-energy X-rays (we assume 1 keV), the cross-section is approximately the Thompson scattering cross-section, σ_T, while for stellar emission we account for some energy dependence in that lower-energy non-ionizing photons may additionally be scattered and attenuated by semi-ionized gas, trace metals, and a trace level of dust (modelled to be present only in 30 per cent of the volume of ISM[5] where it is set to have 1 per cent of the average Milky Way dust fraction; see Section 3.2.4) in the early ISM (see Cruddace et al. 1974), and ionizing photons will scatter in a similar manner to the X-rays.

We assume that all non-ionizing photons have energies equal to the peak energy in the blackbody spectrum ($E_\gamma = 2.82 k_B T_*$) as this is the modal average energy of the photon gas. Considering separately the ionizing radiation, we assume that these photons all have an energy of 13.6 eV, the lowest energy at which they can be ionizing – this is within the Wein part of the spectrum, with most photons at the lower energies, close to the ionization threshold. The fraction of the stellar radiation in the ionizing and non-ionizing part of the spectrum is estimated by numerically integrating the *Planck* function over energy in the two regimes.

While the luminosity of individual stars can be determined using the Stefan–Boltzmann law, as before, the X-ray emission from the galaxy is attributed to a range of sources and processes. For simplicity, we assume a total galactic luminosity of $L_X = 8.3 \times 10^{38}\,\mathrm{erg\,s^{-1}}$, corresponding roughly to a system with $\mathcal{R}_{SN} \approx 0.1\mathrm{yr}^{-1}$ or $\mathcal{R}_{SF} \approx 16\mathrm{M}_\odot\mathrm{yr}^{-1}$ according to scaling relation estimates in the literature (see e.g. Li & Wang 2013; Appleton et al. 2015; Sarkar et al. 2016), and similar to the diffuse X-ray luminosity of the starburst M82 (see e.g. Watson, Stanger & Griffiths 1984). We neglect point source contributions in our model because, at $z = 7$, many source candidates would not have had sufficient time to form in abundance. This total X-ray luminosity is then distributed evenly among the 10 000 MC simulation source points that themselves are weighted by the number according to the underlying density profile from which radiative sources would be expected to form.

The resulting heating effect of stellar photons within the central parts of the protogalactic ISM (where it is strongest) is around $10^{-25}\,\mathrm{erg\,cm^{-3}\,s^{-1}}$ while, for X-rays, the level is a little lower, around $10^{-26}\,\mathrm{erg\,cm^{-3}\,s^{-1}}$ – in both cases, these rates correspond to $\mathcal{R}_{SN} \approx 1.0\mathrm{yr}^{-1}$, or a star-formation rate of around $\mathcal{R}_{SF} \approx 160\mathrm{M}_\odot\mathrm{yr}^{-1}$ (see conversion in Section 3.3.1). As the non-ionizing stellar radiation is attenuated more effectively, this heating rate falls below that due to X-rays outside the galaxy (see Fig. 6 for the full heating profile).

---

[5]This is set to be the same as that estimated for the ISM of the Milky Way, corresponding to the volume fraction expected to be able to harbour trace dust and semi-ionized gas (see e.g. Ferriere 2001; Draine 2011).

3.2.3 Comparison with previous results

While previous works have examined radiative heating rates in protogalaxies, these are usually estimated in the context of balancing cooling rates when a system is assumed to be in thermal equilibrium (see e.g. Baek et al. 2005). Specific studies regarding stellar and X-ray heating mechanisms in protogalaxies are not widespread, and the expected heating rates in such systems do not appear to have yet been established in the literature. In light of the lack of direct comparisons, we instead provide sanity checks of our radiative heating levels by comparison with more local starburst and Galactic-type environments, which we scale appropriately.

In evolved low-redshift galaxies, radiative heating (particularly UV) is reliant on the presence of dust and polycyclic aromatic hydrocarbons (PAHs) which absorb, scatter and reprocess the optical and soft UV radiation, eventually yielding an ISM heating effect (see e.g. Bakes & Tielens 1994; Wolfire et al. 1995; Meijerink & Spaans 2005; Serra, Doré & Lagache 2016; Hu et al. 2017). High-redshift protogalaxies, however, are considerably less abundant in dust and PAHs (see Section 3.2.4), which means that these mechanisms do not efficiently operate. Instead, the main mechanism would be Thompson (Compton) scattering.

In Glover & Clark (2012), heating rates for molecular clouds are considered when illuminated by a galactic-like interstellar radiation field (ISRF) as described in Draine (1978), with cloud densities ranging from 10^1 to $10^6\,\mathrm{cm^{-3}}$. The relevant heating mechanisms are a combination of photo-electric heating by dust extinction, molecular hydrogen (H_2) photodissociation, and the pumping of highly excited vibrational levels of H_2 by UV photons – the 'UV pump' (Burton, Hollenbach & Tielens 1990). In all instances, it is found that photo-electric heating dominates, with a power of around $10^{-25}\,\mathrm{erg\,cm^{-3}\,s^{-1}}$. In our protogalaxy model, the ISM gas is assumed ionized, while the dust fraction is expected to be negligible compared to a local Universe-type galaxy, so none of the heating mechanisms explored in studies of low-redshift molecular clouds would be feasible dominant channels. Moreover, the ISRF would be substantially different, being more intense in a violently star-forming protogalaxy.

Nonetheless, the Glover & Clark (2012) result can be used as a basis for scaling between local and high redshift galaxy environments. This can be done by replacing the interaction cross-section associated with the heating process, and scaling the ISRF to a level appropriate for high redshift galaxies. The cross-section of photo-electric grain heating is taken to be $1.5 \times 10^{-21}\,\mathrm{cm^2}$ (see Draine 1978), about 10^4 times larger than that for Thompson scattering. The total ISRF luminosity in a protogalaxy is about 10^4 times that of the Milky Way, derived from the star counts of the host galaxies (10^6 stars in the protogalaxy compared to 10^{11} stars in the Milky Way), the bolometric luminosities of those stars (type O/B stellar luminosity is around 10^6 times greater than the low mass stars that tend to dominate the Milky Way population; see Ledrew 2001; Lada 2006; Beech 2011) and the volume containing these stars (10^3 times smaller in the protogalaxy). Thus, in the case of pure Thompson scattering (reducing the cross-section by a factor 10^4), and in a protogalactic ISRF (increasing the intensity by a factor of around 10^4), the stellar heating rate in the protogalaxy ISM would be roughly the same as that calculated in the molecular cloud, around $10^{-25}\,\mathrm{erg\,cm^{-3}\,s^{-1}}$, broadly in line with what we find.

There are not many direct comparisons available in the literature for X-ray heating. However, the heating mechanisms are insensitive to the environments. The process of X-ray ionization followed by thermalization through Coulomb interactions of the emitted electron

will arise in any partially ionized medium. The scattering of the free electrons (either in a plasma, or when electrons are emitted after ionisation processes) will also arise in systems where free electrons are present. Complications such as dust scattering and metallicity are less important for X-ray heating than for stellar heating, and so rates in the literature are more broadly comparable to the results of this study. Meijerink & Spaans (2005) find a rate of 10^{-24} erg cm^{-3}s^{-1} for a characteristic starburst environment similar to the one considered in this paper, modelled on NGC 253, with $\mathcal{R}_{SN} \approx 0.1\text{yr}^{-1}$ (Ferriere 2001), but for an ISM density of 10^3 cm^{-3}. As the heating is determined by the density of the target ISM and intensity of the X-rays, it scales accordingly. Therefore, in a 10 cm^{-3} ISM, the X-ray heating power would be around 10^{-26} erg cm^{-3}s^{-1}, which is roughly comparable to that found in Section 3.2.2.

3.2.4 Dust scattering in protogalaxies

Starburst galaxies in the local Universe are rich in dust, presumably from sources such as Asymptotic Giant Branch (AGB) and evolved stars (see e.g. Ferrara, Viti & Ceccarelli 2016, among others). The build-up of dust produced by AGB stars is expected to be on the evolutionary time-scales of the host galaxies, which, in some cases, is comparable to the Hubble time. Dust in protogalaxies in the early Universe is more likely to be a product of SN events resulting from the evolution of massive stars that occurs on a short time-scale; such candidates are core-collapse SNe (see e.g. Gall, Hjorth & Andersen 2011; Bocchio et al. 2016). There are arguments that core-collapse SNe might not be efficient in dust production, as powerful shocks (particularly reverse shocks) in and around core-collapse SN remnants penetrate into the SN ejecta and can destroy much of the dust that would otherwise form (Bianchi & Schneider 2007; Nozawa et al. 2007; Nath, Laskar & Shull 2008; Silvia, Smith & Shull 2010), reducing the abundance considerably (see e.g. Yamasawa et al. 2011). Observations seem to support this, with evidence for considerably less dust in high-redshift galaxies, particularly above $z \approx 5$ (Walter et al. 2012; Ouchi et al. 2013; González-López et al. 2014; Ota et al. 2014; Riechers et al. 2014; Capak et al. 2015; Maiolino et al. 2015; Bouwens et al. 2016), with the exception of quasar host galaxies (Beelen et al. 2006; Michałowski et al. 2010). A recent study (Ginolfi et al. 2018) pointed also to the evolution of the dust content in galaxies as they evolve – there could be a substantial reduction of dust content (by two orders of magnitude) compared to a present-day galaxy (at $z = 0$) when tracing back to its very early stages, e.g. at $z \sim 7$ and a significant reduction of dust content if the metal content in the environment is deficient. The strong scattering and radiative reprocessing effects by dust, which could be important in local starbursts, e.g. M82 (see, among others, Hutton et al. 2014; Gao et al. 2015; Hutton, Ferreras & Yershov 2015), would be unlikely to play an important role in reprocessing starlight in metal poor protogalactic environments in the very early Universe considered in this study. For this work, we therefore assume only a trace dust component in the host ISM.

3.3 Magnetic field

Observations and simulations have indicated that young galaxies may have developed magnetic fields of strengths comparable to those in the current Universe within a few Myr of their formation (Bernet et al. 2008; Beck et al. 2012; Hammond, Robishaw & Gaensler 2012; Rieder & Teyssier 2016; Sur, Bhat & Subramanian 2018). This suggests that there must be mechanisms prevalent

during the early protogalactic stages of galaxy evolution, in which magnetic field amplification mechanisms transformed seed magnetic fields (of around 10^{-20} G; see e.g. Sigl, Olinto & Jedamzik 1997; Howard & Kulsrud 1997) to the saturation magnetic fields of a few μG observed in galaxies today (Beck et al. 2005; Fletcher et al. 2011; Adebahr et al. 2013; Beck & Wielebinski 2013).

3.3.1 Field development in the protogalaxy

A number of mechanisms have been proposed to drive this magnetic field growth, most notably invoking turbulence driven by accretion and SN explosions of early generations of stars (see e.g. Beck et al. 2012; Latif et al. 2013). Schober, Schleicher & Klessen (2013) introduce an appropriate model that demonstrates the evolution of the field according to the onset of turbulence due to rapid star-formation and the resulting high SN rate (Rees 1987; Balsara et al. 2004). The model describes the time-evolution of the protogalactic magnetic fields on two scales: a large-scale field, $B_L(t)$, and a small-scale, viscous field $B_v(t)$. On the viscous scale, the evolution of the magnetic field $\mathcal{Q}(t)$ is modelled by an exponential increase of magnetic field strength from a seed field B_0 (being the weak seed field permeating the protogalaxy before the onset of star formation of strength around 10^{-20} G) to the saturation strength field $B_{v,sat} = \mathcal{S}(\ell_v/L_f)^{\theta} f$ at a growth rate Γ (see Braginskii 1965; Kazantsev 1968) in a time t_v, i.e. $\mathcal{Q}(t) = B_0 \exp(\Gamma t)$, after which the non-linear evolution begins to dominate. Note that θ is introduced here as the slope of the turbulent velocity spectrum, which takes a value of around 1/3 in the case of incompressible turbulence (Kolmogorov 1941), and increases with compressibility. Here, ℓ_v is the viscous scale of the field, $\mathcal{S} = \sqrt{4\pi\rho}v_f$ with v_f as the typical fluctuation velocity of the largest forcing scale L_f sized eddies in the turbulent flow, and $\rho = \rho(r)$ is the local protogalaxy matter density.[6] In the case of SN-driven turbulence in a spherical protogalaxy model as considered here, $v_f \approx R_{gal}(2\pi\rho G/3)^{1/2}$ and $L_f \approx \rho v_f^3/(\mathcal{R}_{SF}\alpha_*\beta\xi\,\epsilon_T E_{SN})$ (Schober et al. 2013). The velocity is estimated from a pressure/gravity equilibrium approximation and the forcing scale L_f is estimated by comparing the energy dissipation rate with the energy input rate due to SNe that is modelled to follow the star-formation rate $\mathcal{R}_{SF}$ via the relation $\alpha_*\beta\,\epsilon_T\mathcal{R}_{SF}/M_{SN}$. Here, $\varepsilon_T \approx 0.1$ is the fraction of energy transferred from the SN to turbulent energy (e.g. Walch & Naab 2015), and $\xi = 0.01$ accounts for the fraction of energy lost by the SN to neutrinos (see equation 41 and the following text for discussion of this parameter and its value). β is introduced as an efficiency parameter specifying the fraction of SN energy transferred into ISM turbulence. α_*, which specifies the fraction of stars produced that ultimately yield an SN, is determined by the initial mass function (IMF) of the stars that form in the galaxy and also M_{SN}, the mass of a star that eventually produces an SN event.

It may be estimated as follows:

$$\alpha_* \approx \frac{\int_{M_{SN}}^{M_{max}} dM\, M^{-\Upsilon}}{\int_{M_{cut}}^{M_{max}} dM\, M^{-\Upsilon}}\,, \tag{32}$$

where we use a value of $M_{SN} = 8.5M_{\odot}$ for the minimum mass progenitor mass for a core-collapse SN event (following e.g. Smith

---

[6]Given our assumption that the magnetic field is predominantly driven by SNe, it follows that its morphology should follow that of the SN population which roughly traces the gas density profile of the galaxy, as accounted for in this term.

et al. 2011),[7] and we adopt an upper limit for the progenitor mass of $M_{max} = 50M_\odot$.[8] To calculate the fraction of stars that yield SN events, we normalize over a mass range from $M_{cut} = 1\ M_\odot$ to $M_{max} = 50\ M_\odot$, which assumes a negligible population fraction of stars with $M > 50\ M_\odot$ (indeed, the power-law nature of the IMF suggests that the fraction of stars with $M > 50\ M_\odot$ would not be more than 1 per cent for any reasonable choice of maximum upper mass). We otherwise use a Salpeter IMF with index $\Upsilon = 2.35$ for deriving a conversion between the SN event rate $\mathcal{R}_{SN}$ and the star-formation rate $\mathcal{R}_{SF}$. This gives $\alpha_* \approx 0.05$ and a conversion of $\mathcal{R}_{SF} \approx 160 M_\odot yr^{-1}(\mathcal{R}_{SN}/yr^{-1})$, which we use throughout this study.

The large-scale evolution of the magnetic field then follows the viscous evolution, scaled by $(\ell_v/L_f)^{5/4}$ until a saturation time t_v, after which large scale turbulent growth dominates the evolution,

$$B_L(r,t) = \begin{cases} \mathcal{Q}(r,t) \cdot \left(\dfrac{\ell_v}{L_f}\right)^{5/4} & [t < t_v] \\ \mathcal{S}(r) \cdot f \cdot \left(\dfrac{\ell_p(t)}{L_f}\right)^{\theta+5/4} & [t_v \leq t < t_{sat}] \\ B_{L,sat}(r) & [t > t_{sat}] \end{cases} . \quad (33)$$

Here, ℓ_p is the scale of peak energy of the magnetic field given by $\ell_v + [v_f(t - t_v)/L_f^\theta]^{1/(1-\theta)}$ (Schober et al. 2013), and the saturation strength is $B_{L,sat}(r) = \mathcal{S}(r)\,f$, where $f = 0.1$ is the fraction of the turbulent kinetic energy transferred to magnetic energy, estimated from simulations (see Federrath et al. 2011).

We can use this formulation to model the magnetic field growth in a starburst protogalaxy based on the star-formation rate (and hence the SN rate). While the star-formation rate in some protogalaxies is believed to be very high, there is little agreement between different theoretical and observational studies (particularly at the high redshifts of interest here) with rates potentially varying from 0.1 $M_\odot yr^{-1}$ in fairly quiescent cases to over 1000 $M_\odot yr^{-1}$ in the most massive examples (Hernquist & Springel 2003; Robertson et al. 2010; Ouchi et al. 2013; Stark et al. 2013; Barger et al. 2014). The rate of star-formation and the rate of CRs produced are related through the rate of SN events. For local starburst galaxies, the SN event rates are estimated to be ~0.1 yr^{-1} for M82 (Fenech et al. 2010) and NGC 253 (Lenc & Tingay 2006) and ~4 yr^{-1} for Arp 220 (Lonsdale et al. 2006). Assuming SN event rates $\mathcal{R}_{SN}$ in the range between 0.1 and 10 yr^{-1} would cover a reasonable fraction of plausible parameter space. Thus, we consider SN rates within this range and assess the magnetic field development and the impact on CR-driven heating power. From the expressions for v_f and L_f, and by setting values for the efficiency parameters $\alpha_* = 0.05$ and $\beta = 0.05$ (based on simulations; see e.g. Latif et al. 2013), we

---

[7]This is consistent with a best-fitting value of around $8 \pm 1 M_\odot$, see Smartt et al. (2009), also Smartt (2009).

[8]The upper limit for the progenitor mass is uncertain and there is some debate in the literature. Values as low as 16.5 $M_\odot$ are proposed in some cases (e.g. Smartt et al. 2009). However, masses of core-collapse progenitor red super-giant stars are observed to exist up to masses of at least 25 $M_\odot$ (see Smith et al. 2011). Moreover, SN Type IIn arise from stars with initial masses of above 40 $M_\odot$ (e.g. Muno et al. 2006; Tominaga et al. 2008), which pushes the core-collapse progenitor mass even higher (see also Smith, Vink & de Koter 2004; Smith, Hinkle & Ryde 2009). Observational studies of M31 and M33 also suggest maximum cut-offs of around 35−45 $M_\odot$ (e.g. Jennings et al. 2014; Díaz-Rodríguez et al. 2018). Since our model is not sensitive to the maximum value adopted for progenitor mass, we simply use the suggested theoretical maximum limit for a progenitor able to yield an SN event (above which direct collapse into a black hole is favoured), of 50 $M_\odot$ (see Fryer 1999; Heger et al. 2003).
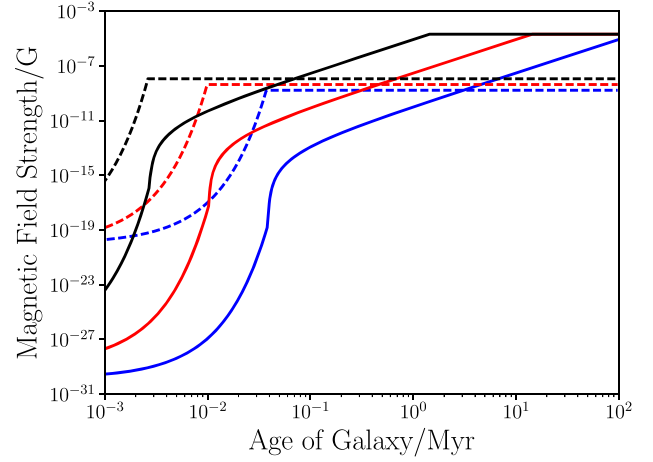
Figure 2. Magnetic field evolution with SN rates of $\mathcal{R}_{SN} = 0.1, 1$ and 10 yr^{-1} (curves in blue, red, and black, respectively). Solid lines indicate the evolution of the large-scale ordered magnetic field, and dashed lines are the evolution for the viscous scale, turbulent magnetic field. This uses values for $\alpha_* = 0.05$ and, based on simulations, $\beta = 0.05$ (Latif et al. 2013).

can specify models describing the development of the protogalactic magnetic field for each SN rate, as per Fig. 2.

3.3.2 CR propagation

In a uniform magnetic field, the gyration of a charged CR particle is characterized by the Larmor radius, which is given by

$$r_L = \frac{3.3 \times 10^{12}}{|Z|}\left(\frac{E}{10^9\,eV}\right)\left(\frac{\mu G}{B}\right)\ cm, \quad (34)$$

where Z is the charge of the particle. Propagation of CR particles in a medium permeated by a tangled magnetic field is more complicated. However, r_L can be used to derive a phenomenological description for CR transport in terms of diffusion, in which the interaction of the particles with the magnetic fields is treated as scattering. In this scenario the CR particles advect and diffuse spatially, subject to radiative energy loss and momentum redistribution until they collide with another particle that results in a cascade of particle production.

In this demonstrative study, we adopt this as our working scenario. Moreover, we consider that energy loss and momentum redistribution of the CR particles are insignificant during particle propagation before the collision with another particle. In a galactic region without a large-scale flow, advective transport is also insignificant. Thus, the transport of CRs is described by a diffusion equation:

$$\frac{\partial n}{\partial t} = \nabla \cdot [D(E, \mathbf{r}, t)\nabla n] + Q(E, \mathbf{r}, t) \quad (35)$$

where $n(E, \mathbf{r}, t)$ is the number density of CR particles with energy E at location $\mathbf{r}$ and time t. The two parameters in the equation are the injection rate of the CR particles, represented by the source function $Q(E, \mathbf{r}, t)$, and the diffusive speed of the particles, expressed in terms of the diffusion coefficient, $D(E, \mathbf{r}, t)$. For the case of spherical symmetry, only the radial component is relevant. Hence, the transport equation becomes

$$\frac{\partial n}{\partial t} = \frac{1}{r^2}\frac{\partial}{\partial r}\left[D(E, r, t)r^2\frac{\partial n}{\partial r}\right] + Q(E, r, t). \quad (36)$$

Without losing generality, we consider only CR protons. The diffusion coefficient takes the parametric form:

$$D(E, r, t) = D_0(t) \left[\frac{r_L(E, \langle B \rangle)|_{r,t}}{r_{L,0}(t_{sat})} \right]^{1/2} \qquad (37)$$

where $\langle B \rangle$ is a characteristic mean magnetic field strength, evaluated at a location r and time t, and t_{sat} is the time at which the galactic magnetic field has evolved to reach a saturation state. Here, the reference Larmor radius $r_{L,0}(t_{sat})$ corresponds to that of a 1 GeV CR proton gyrating around a 5μG uniform magnetic field, and the normalization $D_0(t_{sat}) = 3.0 \times 10^{28}$ cm^2 s^{-1}, a value roughly equal to that which is observed in the Milky Way ISM (see e.g. Berezinskii et al. 1990; Aharonian et al. 2012; Gaggero 2012).

The source function is a product of two separable components:

$$Q(E, r; t) = \left\{ \mathcal{L}_{CR}(E) S_N(r) \right\} \Big|_t \qquad (38)$$

with the energy spectrum of the CR particles given by $\mathcal{L}_{CR}(E)$, and the rate of the CR injection per unit volume represented by $S_N(r)$. As stochastic acceleration generally gives a power-law energy spectrum, $\mathcal{L}_{CR}(E)$ assumes the form

$$\mathcal{L}_{CR}(E) = \mathcal{L}_0 \left(\frac{E}{E_0} \right)^{-\Gamma} . \qquad (39)$$

We set the power-law index $\Gamma = 2.1$, following observations of the galactic differential CR flux power spectrum (see Kotera & Olinto 2011; Kotera, Allard & Olinto 2010; Allard et al. 2007, although we acknowledge that steeper indices of 2.3–2.4 have been suggested more recently in the case of pure proton spectra, e.g. Adrián-Martínez et al. 2016; H.E.S.S. Collaboration 2018). Note that this index corresponds to a flatter spectrum than that of CR electrons that suffer more severe radiative losses (see e.g. Amenomori et al. 2008). Using the lowest energy under consideration in this work, 10^9 eV, as the reference energy E_0 and the maximum energy of interest for CR injection, $E_{max} = 10^{15}$eV, we define the normalization

$$\mathcal{L}_0 = \frac{L_{CR,eff}(1 - \Gamma)E_0^{-\Gamma}}{E_{max}^{1-\Gamma} - E_0^{1-\Gamma}} \qquad (40)$$

where $L_{CR,eff}$ is the power in the CR protons. Supposing that the CR protons are consequential of SN events, then $L_{CR,eff}$ may be expressed as

$$L_{CR,eff} = \varepsilon \xi E_{SN} \mathcal{R}_{SN} = \alpha_* \left[\frac{\varepsilon \xi E_{SN} \mathcal{R}_{SF}}{M_{SN}} \right] . \qquad (41)$$

where $\mathcal{R}_{SN}$ is the SN event rate, E_{SN} is the total energy generated per SN event, M_{SN} is the mass of the SN progenitor star, $\mathcal{R}_{SF}$ is the star-formation rate, α_* is the fraction of stars to yield a SN, ε is the fraction of SN power converted into to CR power and ξ accounts for the fraction of SN energy lost to neutrinos. We assume that $E_{SN} \approx 10^{53}$ erg (the energy output of core-collapse Type II P SNe and hypernovae, that have a massive low-metallicity progenitor), $M_{SN} \sim M_{SN, max} \approx 50 M_\odot$ (i.e. the maximum realistic mass of a

SN event to attain a conservative estimate on the CR luminosity), $\varepsilon \sim 0.1$[9] and $\xi \sim 0.01$.[10]

The following computational scheme is adopted to determine the CR particle density in our model galaxies and how they diffuse outward. CRs are injected as discrete packets, and the total CR power is the sum of all injection episodes. If there are N_S injection packets in total, the spectral energy density of each is simply

$$N_{CR}(E) = \frac{\mathcal{L}_{CR}(E)}{N_S} . \qquad (42)$$

With this prescription, each injection episode is an independent event and hence it serves as the initial condition for the homogeneous diffusion equation,

$$\frac{\partial n}{\partial t} = \frac{1}{r'^2} \frac{\partial}{\partial r'} \left[D(E, r', t) r'^2 \frac{\partial n}{\partial r'} \right] \qquad (43)$$

(with r' as the radial distance from the injection location $\mathbf{r}_s$), governing the evolution of the CR particles after their injection. The diffusion equation with a position-dependent coefficient $D(E, r', t)$ can be solved using the method of Greens' functions.

For the case of a single, discrete injection of duration Δt initiated at $t = 0$, equation (43) gives

$$n(E, r', t) = \frac{N_{CR}(E)|_{\mathbf{r}_s} \Delta t}{[4\pi D(E, r', t) t]^{m/2}} \exp \left\{ -\frac{r'^2}{4D(E, r', t) t} \right\} . \qquad (44)$$

The geometrical parameter here $m = 3$, which corresponds to an injection at a point source and the subsequent diffusion through an infinite volume.[11] The solution for injections at multiple episodes can be obtained by a convolution of the solutions for the individual instantaneous injections. In the continuous limit, the solution[12] is

$$n_T(E, r', t) = \frac{N_{CR}(E)|_{\mathbf{r}_s} t \Gamma(a, b)}{(1 + p) [4\pi D(E, r', t) t]^{m/2}} \left\{ \frac{r'^2}{4D(E, r', t) t} \right\}^{\Upsilon} \qquad (45)$$

where the index is given by

$$\Upsilon = \frac{1}{1 + p} - \frac{m}{2} \qquad (46)$$

---

[9] Recent observational and theoretical studies suggest that a range between 7 per cent (Lemoine-Goumard et al. 2012) and 30 per cent (Fields et al. 2001; Caprioli 2012) would be appropriate for this parameter, with 10 per cent (i.e. $\varepsilon \sim 0.1$) usually being taken as a characteristic value (e.g. Strong et al. 2010; Morlino & Caprioli 2012; Dermer & Powale 2013; Wang & Fields 2018, among others). In line with this, we choose $\varepsilon \sim 0.1$, a conservative estimate within a realistic range of parameter values.

[10] There are great uncertainties of in these parameters. In particular, ξ depends on the types of SNe expected and the ISM environment (see e.g. Iwamoto & Kunugise 2006). Core-collapse SNe have massive progenitors, and most of their energy is carried away by neutrinos. ξ is expected to be around 0.01, although some have argued that it could be as low as 0.001 (see reviews, e.g. Smartt 2009; Janka 2012). For Type 1a SNe, which are less likely to arise in protogalaxies populated by massive young stars, ξ would be reflective of neutrino losses of a few percent (e.g. as per models and simulations in Wright et al. 2017).

[11] For a point source in an infinite plane $m = 2$, and for a point source on a line $m = 1$. The protogalaxy that we model in this paper is not a point source but a collection of sources spherically distributed within. These sources do not interact with each other, and $m = 3$ is applied in deriving the contribution from each individual.

[12] Obtained by Wolfram Mathematica.

and the arguments in the upper incomplete Gamma function $\Gamma(a, b)$ are

$$a = \frac{-2 + m + pm}{2 + 2p} \quad (47)$$

and

$$b = \frac{r'^2}{4D(E, r', t)t} . \quad (48)$$

The parameter p is the index for the late-time evolution of the non-saturated magnetic field, $\propto t^p$. This depends on θ, the slope of the turbulent velocity spectrum (see Section 3.3.1). A value of $p = 2.88$ is appropriate here, but $p = 0$ after the magnetic field growth has saturated.

4 CR HEATING IN PROTOGALAXIES

4.1 Heating rate

4.1.1 Microphysics of energy deposition

CR heating effects are driven by specific interaction channels. For example, γ-rays and neutrinos are relatively weakly interacting, and are unlikely to contribute significantly to local energy deposition or ISM heating. Electrons (also including positrons) are much more instrumental in driving a heating effect and are produced in the decays of secondary charged pionic particles.

The secondary pions produced in the pp process inherit a large fraction of the primary CR energy over a small number of interactions. In a single interaction, secondary pions directly inherit around 60 per cent of the CR primary energy, with the rest leading to secondary neutrons and protons that can undergo further interactions. It can be shown that within just a small number of events of these secondary neutrons and protons, nearly 100 per cent of the primary energy is transferred to pions (see Appendix B) so that instantaneous energy transfer to secondaries at the site of the initial interaction is a reasonable approximation.

The charged pion secondary particles decay to form electrons and positrons (we refer to both of these together as simply 'electrons' for simplicity here) which inherit around 25 per cent of the pion energy (with the rest going into neutrinos, see e.g. Aharonian & Atoyan 2000; Loeb & Waxman 2006; Dermer & Menon 2009; Lacki & Thompson 2012; Lacki & Beck 2013). A single electron-yielding interaction will generally produce more than one electron and, at the mean energy of the CR spectrum used in our model (according to the power-law distribution described in Section 3.3.2) $\bar{E} \approx 2.5$ GeV gives a secondary electron multiplicity of around 4 (when rounded to the nearest integer).[13] As such, the energy transferred from the CR primary to the electrons must be split equally among these secondary particles. For our calculations, we assume that the average multiplicity of 4 is suitable for all energies, as the lower energies of

---

[13]This value is determined empirically by fitting functions to experimental pp-interaction multiplicity data from Breakstone et al. (1984), Slattery (1972), Thome et al. (1977), Ansorge et al. (1989), Rimondi (1993), Alner et al. (1985), Alexopoulos et al. (1998), Albajar et al. (1990), Arnison et al. (1983), Alner et al. (1984), Abe et al. (1990), Whitmore (1974), and Wang (1991). The review paper Fiete Grosse-Oetringhaus & Reygers (2010) and analysis in Albini et al. (1976) find a function of the form $a + bs^{\mathcal{W}}$ provides a good description of the multiplicity data, where s is the centre-of-mass interaction energy (in GeV) and the parameters take values of $a = 0.0$, $b = 3.102$, and $\mathcal{W} = 0.178$ (Fiete Grosse-Oetringhaus & Reygers 2010).

the power-law distribution of comparable multiplicities dominate the interactions. The higher multiplicities associated with higher energy CR interactions do not compensate for the greatly lower abundance of the primaries initiating the secondary cascades when adopting a spectral index of -2.1.

The energy passed to each of the secondary electrons is therefore around 3.75 per cent of the CR primary energy (i.e. 0.6 of the energy is passed to charged pions, of which 0.25 is passed to the electrons, and this is split between an average of around four particles per CR primary), meaning a 1 GeV CR primary would ultimately yield four secondary electrons, each with energies of around 40 MeV. These electrons can then shed their inherited energy via three principal processes: bremsstrahlung, Coulomb interactions (and/or ionization in cool, dense partially ionized plasmas), and radiative cooling, e.g. inverse-Compton scattering off CMB and starlight photons, or synchrotron cooling in the interstellar magnetic fields. Of the radiative cooling mechanisms, inverse-Compton scattering off the CMB and/or starlight dominates in a protogalaxy ISM due to the higher energy density of these radiation fields ($U_{\mathrm{CMB}} \approx 1,100\,\mathrm{eVcm^{-3}}$ at redshift $z = 7$, compared to $U_* \approx 150\,\mathrm{eVcm^{-3}}$, according to equation (A6) with $N = 10^6$ and $NL_* \approx 2.8 \times 10^{44}\,\mathrm{ergs^{-1}}$ for a galaxy with $\mathcal{R}_{\mathrm{SN}} = 0.1\,\mathrm{yr^{-1}}$, and scaling in proportion to SN event rate; see Section 4.1.5) compared to that of the magnetic fields (even when saturated at around 20 μG, $U_{\mathrm{B}} \approx 12\,\mathrm{eVcm^{-3}}$).

The cooling rate due to inverse-Compton scattering with the CMB or starlight takes the form

$$\dot{E}_{\mathrm{rad}} = \frac{4}{3}\sigma_{\mathrm{T}}c\left(\frac{E_{\mathrm{e}}}{m_{\mathrm{e}}c^2}\right)^2 U_i \quad (49)$$

per particle (see e.g. Blumenthal 1970; Rybicki & Lightman 1986) with E_{e} as the energy of the secondary CR electron, and where U_i is the energy density of the radiation field, either the CMB, U_{CMB}, or starlight, U_* (synchrotron cooling takes the same form per particle, with the magnetic field energy density simply substituted for the radiation field energy density). The rate due to bremsstrahlung (free-free emission) per particle may be written as

$$\dot{E}_{\mathrm{ff}} \approx \alpha_{\mathrm{f}}c\sigma_{\mathrm{T}}n_{\mathrm{p}}E_{\mathrm{e}} \quad (50)$$

(see e.g. Dermer & Menon 2009; Schleicher & Beck 2013) where α_{f} is introduced as the fine structure constant, while that due to Coulomb interactions with the ISM (if modelling it as a low-density fully-ionised plasma) is given by

$$\dot{E}_{\mathrm{C}} \approx m_{\mathrm{e}}c^2 n_{\mathrm{p}}c\sigma_{\mathrm{T}}\ln\Lambda \quad (51)$$

(see e.g. Dermer & Menon 2009; Schleicher & Beck 2013) where $\ln\Lambda \simeq 30$ is the Coulomb logarithm accounting for the ratio between the maximum and minimum impact parameters. The relative importance of these processes can be assessed by considering their associated time-scales,
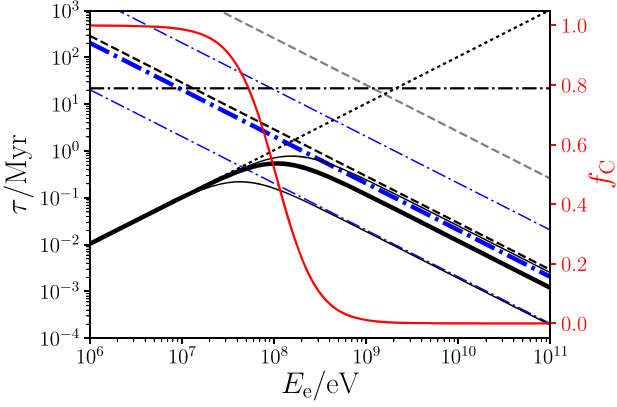
$$\tau = \left|\frac{1}{E_{\mathrm{e}}}\left(\frac{\mathrm{d}E_{\mathrm{e}}}{\mathrm{d}t}\right)\right|^{-1} \quad (52)$$

which can be used to estimate the fraction of energy lost by the CR secondary electron through the respective process.

In terms of thermalization, the ISM heating by the electrons is predominantly driven by Coulomb interactions. The energy of the CR primary ultimately passed into ISM heating is given by the product of f_{e} (being the fractional branching ratio associated with the formation of charged electron secondaries) and $f_{\mathrm{C}}(E_{\mathrm{e}})$, being the fraction of energy lost by secondary electrons to heating the ISM

Figure 3. Energy loss time-scales for CR secondary electrons with energy E_e: Coulomb (black dotted line), radiative inverse-Compton losses with the CMB (black dashed line) and stellar radiation fields (blue dashed lines – the thickest due to the radiation field resulting from a protogalaxy model with $\mathcal{R}_{SN} = 1\,\mathrm{yr}^{-1}$, the upper line for $\mathcal{R}_{SN} = 0.1\,\mathrm{yr}^{-1}$, and the lower line for $\mathcal{R}_{SN} = 10\,\mathrm{yr}^{-1}$), radiative synchrotron in saturated protogalactic magnetic field (dashed grey line), free–free bremsstrahlung (black dotted-dashed line). The solid black line shows the total energy loss -, the thick line in the case of the stellar radiation field with $\mathcal{R}_{SN} = 1\,\mathrm{yr}^{-1}$ and thin lines for the other stellar radiation field models. The solid red line shows the thermalization efficiency, f_C, which is the fraction of CR electron energy transferred by the Coulomb-driven thermalization process to the ISM compared to other processes. Below $E_e = 10^7\,\mathrm{eV}$ this is approximately 1.0, indicating almost full thermalization while, above $E_e = 10^9\,\mathrm{eV}$, f_C becomes very small, indicative of inefficient thermalization with most CR electron secondary energy lost to other processes. This assumes an ISM density of $n_p = 10\,\mathrm{cm}^{-3}$.

through Coulomb processes, given by

$$f_C(E_e) = \left.\frac{\tau_C^{-1}}{\tau_C^{-1} + \tau_{\mathrm{rad}}^{-1} + \tau_{\mathrm{ff}}^{-1}}\right|_{E_e} \tag{53}$$

with τ_C, τ_{rad}, and τ_{ff} as the Coulomb, radiative (inverse-Compton and synchrotron), and free-free (bremsstrahlung) cooling time-scales for the CR secondary electrons, respectively. The total fraction of CR primary energy E which is thermalized into the ISM then follows as $f_{\mathrm{therm}}(E) = (\xi_e f_C f_e)|_{E_e}$ for ξ_e as the electron production multiplicity (we use $\xi_e = 4$ and $E_e = 0.0375E$). The energy dependence of the time-scales (plotted in black) and the resulting impact this has on the Coulomb thermalisation fraction (i.e. f_C - plotted in red) are shown in Fig. 3, where the time-scales and thermalization fractions are shown in terms of the CR secondary energy, E_e. Here, it is apparent that the lower energy secondaries (arising from 1–10 GeV primaries) are much more important in driving ISM heating process than higher energy particles for which the losses are largely dominated by the radiative processes that are less directly involved in heating the local environment. Equations (49)–(51) also indicate a dependency on the local matter density (i.e. on the environment), and this is further explored in Fig. 4, where, again, time-scales are shown with black lines, and the Coulomb thermalization fraction is shown in red. Here, it follows that higher densities provide a much more effective heating target while CRs are less efficiently thermalized by this mechanism in lower density environments.

4.1.2 Individual sources

As CR particles are highly relativistic, their speeds approach the speed of light, c. The rate of heating per unit volume by the particles through hadronic interactions at a location r' from an individual
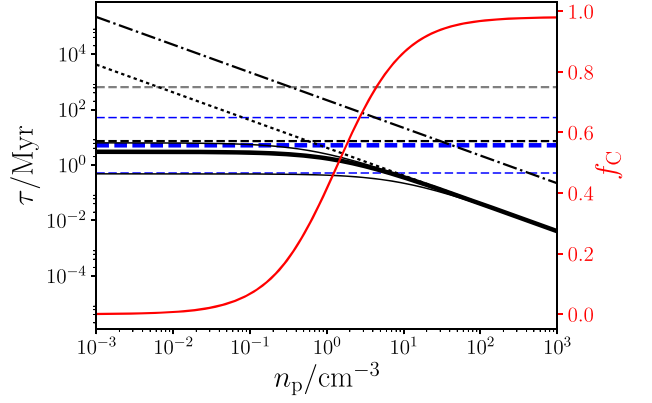
Figure 4. Energy loss time-scales for CR secondary electrons over different ISM densities: Coulomb (black dotted line), radiative inverse-Compton losses with the CMB (black dashed line) and stellar radiation fields (blue dashed lines – the thickest due to the radiation field resulting from a protogalaxy model with $\mathcal{R}_{SN} = 1\,\mathrm{yr}^{-1}$, the upper line for $\mathcal{R}_{SN} = 0.1\,\mathrm{yr}^{-1}$ and the lower line for $\mathcal{R}_{SN} = 10\,\mathrm{yr}^{-1}$), radiative synchrotron in saturated protogalactic magnetic field (dashed grey line), free-free bremsstrahlung (black dotted-dashed line). The solid black line shows the total energy loss time-scales, the thick line in the case of the stellar radiation field with $\mathcal{R}_{SN} = 1\,\mathrm{yr}^{-1}$ and thin lines for the other stellar radiation field models. The solid red line shows the thermalization efficiency, f_C, which is the fraction of CR electron energy transferred by the Coulomb-driven thermalization process to the ISM compared to other processes. Below $n_p = 10^{-2}\,\mathrm{cm}^{-3}$ the value of f_C is very small, suggesting CR heating is very inefficient. Above $10^1\,\mathrm{cm}^{-3}$, it is approximately 1.0, indicating almost full thermalization. This assumes a CR secondary electron initial energy of $E_e = 40$ MeV, approximately corresponding to a CR primary proton energy of around 1 GeV.

source is

$$H(r')|_t = \int_{E_{\mathrm{min}}}^{E_{\mathrm{max}}} \mathrm{d}E\,\mathcal{A}(r')\,n_T(E, r', t)\,c\,\alpha(E, r') \tag{54}$$

i.e. with $n_T(E, r', t)c$ giving the rate at which CRs pass through a surface at r'. The absorption coefficient $\alpha(E, r')$ is the sum of the contributions from all interaction channels of all target particle species, i.e.

$$\alpha(E, r') = \sum_x f_C(E)\,n_x(r')\,\sigma_x(E) \tag{55}$$

where $n_x(r')$ is the number density of target particles of species x and $\sigma_x(E)$ is their corresponding interaction cross-section. $f_C(E)$ results from the microphysics considerations in Section 4.1.1, and $\mathcal{A}(r')$ is a mean attenuation term resulting from the absorption of CRs along their propagations (see Section 4.1.3 for details).

4.1.3 Monte Carlo simulation

Equations (45) and (54) determine the heating contributed by a single CR source. The sources are independent, and hence the heating at a location is the linear sum of the contributions of all sources in the system. This formalism lends itself efficiently to computing the heating using a Monte Carlo method.

We consider a weighted Monte Carlo scheme in which a total number of N_S sources are generated, with their spatial distribution weighted according to the density profile of the protogalaxy up to its characteristic edge (set to be 1 kpc). The size of an individual source is set to be 0.01 kpc, cf. the characteristic size of SN remnants (see e.g. Badenes, Maoz & Draine 2010). This, together with the

efficiency of CR production scaled according to the star-formation rate, provides the initial condition and hence the normalization for equation (45). We adopt a value of $N_S = 10^4$, which, we find, yields an acceptable signal-to-noise ratio in the resulting simulated CR density profile. The spatial density distribution of the target baryons involved in calculating the hadronic interactions follows the density profile of the galaxy.

The absorption of CRs along their propagations due to pp interactions is encoded in equation (54) by the term $\mathcal{A}(r')$. While the attenuation experienced by free-streaming radiation can be calculated according to the optical dept, τ_{free}, that of CRs undergoing diffusive propagation through their attenuating medium takes a modified form. While the CRs propagate on a microscopic level at the speed of light, c, their macroscopic propagation appears to be much slower than this due to the strong magnetic scattering they experience. As such, they will encounter a much greater amount of attenuating material over a given distance than freely streaming particles and the effective CR optical depth must be adjusted accordingly, i.e. $\tau_{\text{CR}}^*(r') = \psi(r')\tau_{\text{free}}(r')$ for $\psi(r')$ as the scale factor. These quantities are calculated locally: i.e. indicating the optical depth experienced by a particle propagating through an infinite medium with the properties at the point r'.

In the free-streaming limit, the time-scale associated with absorption due to the pp interaction is

$$t_{\text{p}\pi} = \frac{\ell_{\text{p}\pi}}{c} = \frac{1}{c n_\text{p} \hat{\sigma}_{\text{p}\pi}} \ . \tag{56}$$

Over such a time-scale, a particle in the diffusion limit would macroscopically be displaced by a characteristic distance

$$\ell_{\text{diff}} = \sqrt{4D t_{\text{p}\pi}} = \sqrt{\frac{4D}{c n_\text{p} \hat{\sigma}_{\text{p}\pi}}} \tag{57}$$

although, when considering the microphysical scatterings, its actual path length would be the same as $\ell_{\text{p}\pi}$ in equation (56) – just compressed into a much smaller region due to the scattering to give a reduced macroscopic displacement. It therefore follows that the same level of attenuation would be experienced (i.e. with the same optical depth) after a particle has propagated a length $\ell_{\text{p}\pi}$ in the free-streaming regime, or ℓ_{diff} in the diffusion regime. The ratio between these path lengths therefore gives the level of additional attenuation that would arise in the diffusion regime compared to a free-streaming particle travelling in a straight line, i.e.

$$\psi(r') = \frac{\ell_{\text{p}\pi}}{\ell_{\text{diff}}} = \sqrt{\frac{c}{4D n_\text{p} \hat{\sigma}_{\text{p}\pi}}} \ . \tag{58}$$

As such, the attenuation can be calculated in the free-streaming limit, and the optical depth scaled by $\psi(r')$ to estimate the attenuation experienced by the CRs in the diffusion regime. The calculation itself is done by considering the path lengths between the heating position r' and each of the sources in the ensemble of N_S MC sources. The free-streaming attenuation along each line of sight is then estimated and adjusted by ψ such that the resulting attenuation factor is

$$\mathcal{A}(r') = \exp\left[-\tau_{\text{CR}}^*(r')\right] = \exp\left[-\psi(r')\tau_{\text{p}\pi}(r')\right] \ . \tag{59}$$

4.1.4 Results

We consider protogalaxies that would be present at redshift $z \approx 7$. These represent the most distant galaxies to be observed in the near future, e.g. in the ultra-deep field of the Subaru HSC deep-field survey (The HSC Collaboration 2012). Fig. 5 shows the evolution
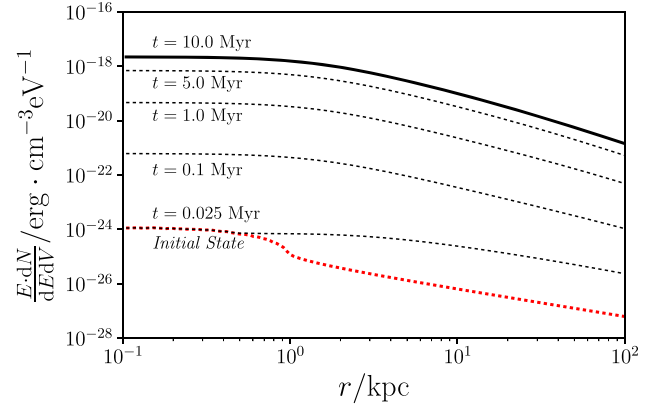
Figure 5. The evolution of the CR profile (at $\bar{E} \approx 2.5$ GeV) with the protogalactic magnetic field for SN rate $\mathcal{R}_{\text{SN}} = 1.0\,\text{yr}^{-1}$ (i.e. our intermediate model in terms of SN rate). The red dashed line corresponds to the initial free-streaming state, while the solid black line corresponds to the steady state profile in which the magnetic field evolution has saturated (by around 10 Myr). The black dashed lines correspond to the interim stages at $t = 0.025$, 0.1, 1.0 and 5.0 Myr, as labelled.

of the CR density distribution (at $\bar{E} \approx 2.5$ GeV) in the protogalaxy when adopting a uniform SN event rate $\mathcal{R}_{\text{SN}} = 1\,\text{yr}^{-1}$. Initially, the galactic magnetic field is not strong enough to confine the CRs, and the energetic charged particles freely stream across the galaxy until they hit a target particle in the ISM, or the IGM, at which point they are destroyed. After a Myr or so, containment of CRs sets in as the magnetic field in the galaxy gains substantial strength. After around 10.0 Myr, the magnetic field evolution has reached saturation and the CR density profile converges to a steady state. As the CR particle number density is linearly scaled with the SN event rate (equation 41), the normalization of the steady-state profile (in Fig. 5) is also linearly scaled with the SN event rate (and hence also the star-formation rate) of the host galaxy.

We calculate the heating power of CRs in these galaxies and assess them as CR calorimeters as their galactic magnetic fields evolve (see Thompson et al. 2007; Lacki et al. 2011). Fig. 6 shows the profiles of the CR heating power for three SN event rates ($\mathcal{R}_{\text{SN}} = 0.1$, 1, and 10 yr^{-1}) in the initial (free-streaming) stage and the later steady-state stage when the evolution of the galactic magnetic field has saturated. For comparison, we also compute the heating power due to starlight and diffuse X-rays as per the prescriptions described in Section 3.2.2, where lines correspond to models with $R_{\text{SN}} = 1.0\,\text{yr}^{-1}$, or to a star-formation rate of around 160 M$_\odot$yr^{-1} by the relation $\mathcal{R}_{\text{SF}} \approx 160\text{M}_\odot\text{yr}^{-1}(\mathcal{R}_{\text{SN}}/\text{yr}^{-1})$ (see Section 3.3.1). For the initial stage, the CR heating profiles are shown spanning from the inner region to beyond the the galaxy. For the steady-state stage, only the profile segments for the region within the ISM of the protogalaxy are shown. In this region CR transport is facilitated mainly by diffusion. Far beyond this central region, the CR particles are practically free-streaming, and the heating rate level is expected to drop off to approximately that of the initial stage. The transitional region in the outskirts of galaxy is less straightforward to model. The CR transport and heating effect depends strongly on the morphological structure of the magnetic field. The time-dependent magnetic activity in the region and the interface between the magnetic ISM and the magnetic IGM is not well understood, so the magnetic field properties in these galactic outskirts are very uncertain. Furthermore, the formulation of a kinetic description of particles in the transition from a diffusion regime to a free-streaming
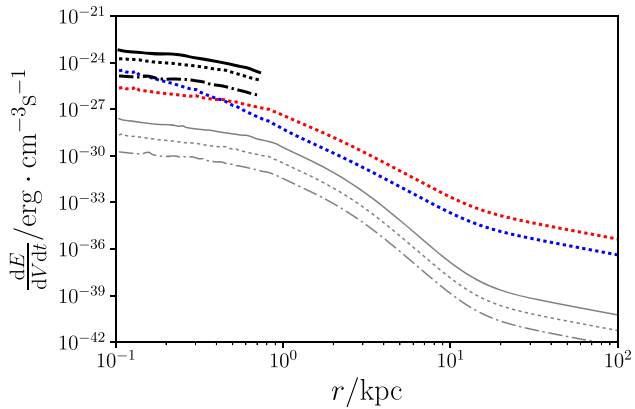
Figure 6. CR heating profiles for SN event rates at $\mathcal{R}_{SN} = 0.1$, 1 and 10 yr^{-1} (dot-dashed, dotted, and solid lines respectively) before (in grey) and after (in black) containment of the CRs by the galactic magnetic field. The profiles for radiative heating by starlight and X-rays are shown in blue and red respectively, corresponding to $\mathcal{R}_{SN} = 1.0$ yr^{-1}, or to a star-formation rate of around 160 M$_{\odot}$ yr^{-1} by the relation $\mathcal{R}_{SF} \approx 160$ M$_{\odot}$ yr^{-1} ($\mathcal{R}_{SN}$/yr^{-1}) (see Section 3.3.1). For CR heating in the presence of magnetic field confinement, only the profile segments for the region within the inner parts of the galaxy are shown. The CR heating rate is expected to fall back down to values similar to those of the free-streaming cases in regions outside the galaxy at distances beyond 10 kpc.

Table 1. Energy densities of CRs ε_{CR} in the Milky Way, M31 and three starburst galaxies M82, NGC 253, and Arp 220. Data were taken from Ferrière (2001) for the Milky Way and from Abdo et al. (2010) for M31. The others are obtained by Yoast-Hull et al. (2016). The results for the three models are for the case with full magnetic containment of the CRs as calculated for the stated SN rates. [1] Estimated from γ-ray observations. If combined with radio data, the CR density is then about $430 - 620$ eV cm^{-3}. [2] Taking the full range of values across different regions of Arp 220 as in the study by Yoast-Hull et al. (2016).

Source	CR energy density / eV cm^{-3}
Milky Way	1.4
M31	1.5
M82	550 [1]
NGC 253	260–350
Arp 220	1100–5100 [2]
Model: 0.1 SN yr^{-1}	350
Model: 1 SN yr^{-1}	3500
Model: 10 SN yr^{-1}	35 000

in dust, which is unlikely to play as important a role in high-redshift starbursts than their low-redshift counterparts. See Section 3.2.4 for further details.

4.1.5 Energetics

The total radiative stellar and X-ray powers are around 2.8×10^{44} erg s^{-1} and 8.3×10^{38} erg s^{-1}, respectively, while that going into the CR primaries is around 3.0×10^{40} erg s^{-1}, i.e. 4 orders of magnitude less than the stellar radiation. The corresponding total power deposited into the ISM in the model is calculated to be 1.9×10^{38} erg s^{-1} and 2.6×10^{37} erg s^{-1} for stellar radiation and X-rays, respectively while, for contained CRs, the heating power to the ISM is 2.1×10^{39} erg s^{-1}, or 7.5×10^{32} erg s^{-1} in the free-streaming case (i.e. consistent with the $\sim 10^{6}$ level of CR containment within the galaxy). All these quoted values are for the conservative case, i.e. for $\mathcal{R}_{SN} = 0.1$ yr^{-1} (or around $\mathcal{R}_{SF} = 16$ M$_{\odot}$ yr^{-1} by the transformation between the two quantities from Section 3.2.2), but are found to scale directly with SN (or SF) rate. The radiative (X-ray) heating power is around 4 orders of magnitude larger than that of the free-streaming CRs. However, when the containment of the CRs is established, it consistently follows that the radiative heating effect becomes sub-dominant, with the CR heating increasing by a factor of around 10^{6}, to 2 orders of magnitude above the X-ray power.

4.2 Discussion

4.2.1 Comparison with nearby galaxies

Multiplying the value of $E dN/dE dV$ in the steady state CR profile (i.e. that in Fig. 5) with the mean energy of CRs $\bar{E}$ with energies above 1 GeV (≈ 2.5 GeV) gives an estimate for the CR energy density ε_{CR} in the model galaxies. We show the results for three cases with SN event rates $\mathcal{R}_{SN} = 0.1$, 1 and 10 yr^{-1} in Table 1. Although, at present, we cannot be certain of the level of CR diffusion or containment in high-redshift galaxies, comparison with values from observations of nearby examples offers some useful insight. Yoast-Hull, Gallagher & Zweibel (2016) have derived the CR energy densities for nearby galaxies, including for the starbursts M82, NGC 253, and Arp 220. The CR energy densities of these three starbursts along with the Milky Way (data from Ferrière 2001), and M31 (data from Abdo et al. 2010) are also included in Table 1 for comparison.

regime (as would arise in these outskirt regions) is theoretically challenging. It deserves an independent study in its own right, and so we leave this to a more thorough future investigation.

The development of the magnetic field leads to the suppression of the free-streaming propagation of CRs, and the subsequent particle confinement leads to an amplification of the CR heating effect. Without CR containment, the ISM is mainly heated by starlight and supplemented by the diffuse X-rays. However, CR heating begins to dominate shortly after the onset of violent star formation. At the time the steady state is reached (by around 10 Myr), the CR heating rates are 10^{-25}, 10^{-24}, and 10^{-23} erg cm^{-3} s^{-1} [14] for $\mathcal{R}_{SN} = 0.1$, 1, and 10 yr^{-1}, respectively, i.e. higher than the rates resulting from heating by starlight and diffuse X-rays. In the most intensely star-forming model, the final CR heating rate attained is slightly lower than might be expected from a direct scaling with $\mathcal{R}_{SN}$. This is due to the comparatively elevated inverse-Compton loss rates of the secondary CR electrons and resulting lower heating efficiency, which arises from the higher intensity of the stellar radiation field in this case. Note that some caution is required when comparing the CR and starlight heating with the X-ray heating. Fig. 6 shows the X-ray heating corresponding to the case where the total X-ray power is 8.3×10^{38} erg s^{-1}. The normalization of the profile for diffuse X-ray heating is scaled with the total power of the X-rays. Thus, the conclusion above should be modified if a higher value for the total X-ray power is adopted. For instance, if the X-ray power is around 8.3×10^{41} erg s^{-1}, X-ray heating will exceed starlight heating in the central 1 kpc of the galaxy. If the X-ray power reaches around 8.3×10^{42} erg s^{-1}, then X-ray heating will become comparable to CR heating for an SN event rate $\mathcal{R}_{SN} = 0.1$ yr^{-1}. We note that these radiative heating rates do not account for scattering or reprocessing

---

[14]These rates are substantially lower than those presented in Owen et al. (2017), in which the heating effect was greatly overestimated as the attenuation of CRs across the galaxy was not properly taken into account and the CR injection rate was overstated.

The CR energy density ε_{CR} obtained for the model with $\mathcal{R}_{SN} = 0.1\,\mathrm{yr}^{-1}$ agrees well with the observed values of M82 and NGC 253, which have an SN rate of $\sim 0.1\,\mathrm{yr}^{-1}$ (Lenc & Tingay 2006; Fenech et al. 2010). The CR energy density ε_{CR} obtained for the model with $\mathcal{R}_{SN} = 1\,\mathrm{yr}^{-1}$ is also consistent with the observed value of Arp 220, which has an SN rate of $\approx 4\,\mathrm{yr}^{-1}$ (Lonsdale et al. 2006). Although the model with the highest SN rate, at $10\,\mathrm{yr}^{-1}$, yields a CR energy density considerably higher than the three nearby starburst galaxies, such an active galaxy may be representative of some of the most violent starburst protogalaxies present in the very distant Universe. By comparison, the Milky Way and M31 are expected to have very low CR energy densities due to a relatively low level of star-formation activity, corresponding to a low SN event rate of $\sim 0.015\,\mathrm{yr}^{-1}$ (see Dragicevich, Blair & Burman 1999; Diehl et al. 2006; Hakobyan et al. 2011; Adams et al. 2013). With such a rate, a direct scaling with the model with $\mathcal{R}_{SN} = 0.1\,\mathrm{yr}^{-1}$ would suggest $\epsilon_{CR} \sim 53\,\mathrm{eV\,cm^{-3}}$, more than an order of magnitude higher than the measured value for the Milky Way, at $1.4\,\mathrm{eV\,cm^{-3}}$. This discrepancy arises as a scaling is required to geometrically account for the difference in the sizes of the galaxies. We may resolve this issue as follows: Take the steady-state form of equation (36) and integrate it (by the divergence theorem). From equation (41), we then obtain by dimensional analysis

$$4\pi R^2 \left(\frac{D}{R}\right) n = \kappa \mathcal{R}_{SN}, \tag{60}$$

where κ is some variable specifying the efficiency of CR production in an SN event. This gives a more rigorous scaling relation as

$$\epsilon_{CR,2} = \epsilon_{CR,1} \left(\frac{\mathcal{R}_{SN,2}}{\mathcal{R}_{SN,1}}\right) \left(\frac{D_1}{D_2}\right) \left(\frac{R_1}{R_2}\right) \left(\frac{\kappa_2}{\kappa_1}\right) \left(\frac{\bar{E}_2}{\bar{E}_1}\right). \tag{61}$$

Assuming that diffusion coefficients $D_1 \approx D_2$, the CR conversion variables $k_1 \approx k_2$ and the mean CR energies $\bar{E}_1 \approx \bar{E}_2$, we obtain $\epsilon_{CR,2} \approx 1.5\,\mathrm{eV\,cm^{-3}}$ if we set $\epsilon_{CR,1} = 350\,\mathrm{eV\,cm^{-3}}$, $R_1 = 1\,\mathrm{kpc}$, and $\mathcal{R}_{SN,1} = 0.1\,\mathrm{yr}^{-1}$ for the reference galaxy and $R_2 = 30\,\mathrm{kpc}$ (see Xu et al. 2015) and $\mathcal{R}_{SN,2} = 0.015\,\mathrm{yr}^{-1}$ for the Milky Way. The CR energy density derived from the model and the measured value of the Milky Way thus reconcile.

4.2.2 Comment on the locality of CR heating

Generally, for CR particle transportation, diffusion arises both in momentum (energy) space and in physical space. Diffusion of charged particles in momentum space is usually caused by radiative or scattering processes. Hadrons are inefficient emitters, thus their radiative loss time-scales are considerably longer than those of other relevant processes. In galactic ISM environments, the time-scale of hadronic CR diffusion through momentum space is expected to be much greater than the time-scale of spatial diffusion (Ko, personal communication, 2017) or advection. The energy loss of a stream of CR particles is therefore dominated by particle attenuation, such as that resulting from hadronic interactions. In the centre-of-momentum frame, the secondary particles resulting from a hadronic interaction have lower energies and shorter mean-free paths (particularly when accounting for magnetic scattering) than their parent particles and we have shown that few interactions are required to entirely convert a hadronic primary into secondary pions (which decay to electrons and neutrinos). We note that neutrinos can only interact weakly so the amount of energy they can deposit in the protogalactic ISM or the IGM is insignificant. Thus the thermalization process is entirely governed by the electronic secondaries,

principally through Coulomb interactions and so the electron thermalization time-scale is estimated by the Coulomb time-scale.

A 1 GeV CR primary proton produces secondary electrons of energy $E_e \approx 40\,\mathrm{MeV}$. In a $10\,\mathrm{cm^{-3}}$ ionized ISM, the thermalization time-scale of these electrons then follows as

$$\tau_{th} \approx 0.39 \left(\frac{E_e}{40\,\mathrm{MeV}}\right) \left(\frac{n_p}{10\,\mathrm{cm^{-3}}}\right)^{-1} \mathrm{Myr}. \tag{62}$$

If the secondary electrons propagated as freely-streaming particles with velocities close to the speed of light, c, this would correspond to a thermalization length-scale of around 0.1 Mpc – considerably larger than the protogalactic host of characteristic radius 1 kpc. However, like the CR primaries, the secondary electrons are charged and their propagation in the magnetic field of the host is also more appropriately modelled as a diffusion process. The diffusion coefficient takes the same form as that for protons that, as the electrons are still relativistic when at tens of MeV, remains in its mass-independent form (see e.g. Kulsrud 2005). The thermalization length, ℓ_{th}, can therefore be estimated as the diffusion length arising over the time-scale τ_{th}, i.e.

$$\ell_{th} \approx \sqrt{4D\tau_{th}}$$

$$\approx 0.17 \left(\frac{E_e}{40\,\mathrm{MeV}}\right)^{3/4} \left(\frac{n_p}{10\,\mathrm{cm^{-3}}}\right)^{-1/2} \mathrm{kpc}. \tag{63}$$

This shows ℓ_{th} to be around an order of magnitude smaller than the characteristic size of the protogalaxy and so demonstrates that the CR energy is generally deposited well within the host. As such, we argue that it is sufficient to model the energy deposition as local to the initial CR interaction. Fully propagating the thermalization lengths of the CR secondaries would simply spread the heating through a volume that remains well within the host's ISM, and so would not substantially alter the results of our calculation. Indeed, we note that the thermalization length-scale is comparable to the resolution of our simulation anyway. In a model with sufficient resolution and explicitly accounting for the thermalization length of the secondaries, differences from our present results would only emerge when ISM density substructures are included in the calculation – in particular if modelling the thermalization within dense clouds compared to the hot, low-density component of the ISM. However, such matters fall beyond the scope of this paper, and are instead left to follow-up work.

In Fig. 7, we plot the thermalization fraction of a beam of secondary CR electrons ε_{th} over their diffusive propagation distance ℓ_{diff} from their initial point of injection (i.e. the location of the initial CR primary interaction) for three energies and ISM densities. The reference case is given by a solid black line, appropriate for the protogalaxy model in this paper for CR electron secondaries of $E_e = 40\,\mathrm{MeV}$ in an ISM of density $n_p = 10\,\mathrm{cm^{-3}}$. The dashed and dotted black lines then give the thermalization fraction over distance for $E_e = 4\,\mathrm{MeV}$ and $400\,\mathrm{MeV}$ electrons, respectively, while the dashed and dotted red lines show the result for $40\,\mathrm{MeV}$ electrons in a medium of $n_p = 1.0\,\mathrm{cm^{-3}}$ and $100.0\,\mathrm{cm^{-3}}$, respectively. This demonstrates the important trends outlined earlier in Section 4.1.1: that higher energy CRs thermalize less efficiently (with ε_{th} reaching less than 0.2 for the 400 MeV CR electrons) and do so over longer distances, and that CRs propagating though higher density environments thermalize more efficiently and more quickly – as indicated by the red dotted line where a 40 MeV CR in a medium just 10 times more dense than the reference model is able to thermalize very locally, within just a few tens of pc.
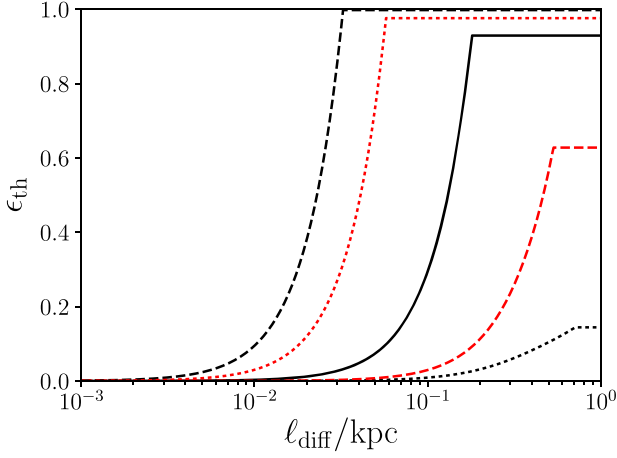
Figure 7. Thermalization fraction of a beam of CR secondary electrons along their diffusive propagations – this gives the fraction of the beam energy thermalized over a specified distance from a source. The reference (solid black) line gives the case for $E_e = 40$ MeV electrons traversing an ISM of density $n_p = 10.0$ cm^{-3}. The dashed and dotted black lines then give the thermalization fraction for $E_e = 4$ and 400 MeV electrons, respectively, while keeping the density fixed at $n_p = 10.0$ cm^{-3}. The red lines show the result for 40 MeV electrons in a medium of $n_p = 1.0$ cm^{-3} (dashed) and 100.0 cm^{-3} (dotted), respectively. Incomplete thermalization of the beam (indicated by a plateau) shows the action of some electron energy loss by free-free and radiative processes, which do not directly contribute to the thermalization process. The maximum thermalization fractions achieved in each case (where the line plateaus) may also be read from Figs 3 and 4. This uses stellar radiation fields consistent with $\mathcal{R}_{SN} = 0.1$ yr^{-1}.

4.2.3 Escape in a CR wind

In Section 4.1.4, we found large increases in CR energy density could arise in the case of their magnetic containment in a protogalaxy ISM. If this is sufficient to yield a pressure gradient able to overcome the gravitational potential of the galaxy, then a galactic wind would erupt able to eject CRs into intergalactic space and drive an outflow. This could substantially reduce the number of CRs that could be harboured inside the host. It is therefore important to establish whether such a CR-driven wind would emerge and, if so, whether it would have the potential to substantially reduce CR containment within the protogalaxy.[15]

We model the wind as a conic section of a spherically symmetric outflow of a hydrogen fluid of density $\rho = m_p n_p$ and adiabatic index $\gamma_g = 5/3$. The momentum equation governing the fluid flow is

$$\frac{q}{r^2} \frac{dv}{dr} = -\frac{dP_c}{dr} - q \frac{GM(r)}{vr^4} \quad (64)$$

where $q = \rho v r^2$ is the mass flow per unit time and P_c is the CR pressure. The adiabatic index of the CRs is $\gamma_c = 4/3$. The energy

---

equation is

$$\frac{1}{r^2} \frac{d}{dr} \left[\frac{qv^2}{2} \right] = -q \frac{GM(r)}{r^4} + I \quad (65)$$

and the energy evolution of the CRs is given by

$$\frac{1}{r^2} \frac{d}{dr} \left[\left(\frac{\gamma_c}{\gamma_c - 1} \right) P_c v r^2 \right] = -I \quad (66)$$

(Ipavich 1975; Drury & Falle 1986; Samui, Subramanian & Srianand 2010; Salem & Bryan 2014) where the interaction term I introduced here quantifies the energy interchange between the CRs and the wind fluid. Without losing generality, we obtain the Bernoulli equation by combining equations (65) and (66)

$$\frac{qv^2}{2} + \left(\frac{\gamma_c}{\gamma_c - 1} \right) P_c v r^2 - q \frac{GM_{gal}}{r} = C_e \quad (67)$$

(Breitschwerdt, McKenzie & Voelk 1991; see Samui et al. 2010) with M_{gal} introduced as the total galaxy mass, i.e. the convergent value of $M(r)$, and C_e being a constant determined by the boundary condition. The CR pressure relates to the CR energy density as $P_c = (\gamma_c - 1)\varepsilon_{CR}$. It follows that[16]

$$\frac{dv}{dr} = \frac{2v}{r} \frac{\left[1 - \frac{GM(r)}{2rc_s^2} \right]}{\left[\frac{v^2}{c_s^2} - 1 \right]} \quad (68)$$

which enables the velocity of a cold, CR-driven wind against gravity to be found. In the equation above, c_s is the effective sound speed. For a CR dominated system,

$$c_s^2 \approx \frac{\gamma_c P_c}{\rho} \approx \frac{\gamma_c \epsilon_{CR}}{3\rho} . \quad (69)$$

The wind velocity is asymptotic to a terminal speed as $r \to \infty$. Such a wind is supersonic past its critical point, and the sound speed must then be faster than the escape velocity v_{esc} (the topology of the different types of solution are explored in, e.g. Recchia, Blasi & Morlino 2016). In equation (67) (the Bernoulli equation), the constant C_e can be evaluated at a reference point, e.g. the critical radius where the outflow becomes supersonic, and at $r \to \infty$ (Breitschwerdt et al. 1991). Assuming that the gravitational potential and the CR pressure as $r \to \infty$ are both substantially less than that at the critical point, equation (67) can be reduced to allow the asymptotic cold CR-driven wind velocity (hereafter the 'terminal velocity') to be estimated as

$$v_{CR,\infty}^2 \approx \frac{2c_s^2}{(1 - \gamma_c)} - v_{esc}^2 \quad (70)$$

(Breitschwerdt et al. 1991) where $v_{esc}^2 = GM_{gal}/r$. We take the wind terminal velocity, $v_{CR,\infty}$, as an upper limit for the rate at which CRs can leak out of the protogalaxy. From this, the CR escape time-scale associated with any resulting wind, should one arise, can be estimated for the different CR energy densities and compared to the diffusion time-scale for a given model. If the diffusion time-scale is substantially shorter, then the CRs propagate predominately by diffusion and are effectively contained in the galaxy. If the wind escape time-scale is shorter, then the CRs are able to effectively leak out of the host, and the containment picture no longer holds. For interim cases, where the time-scales are comparable, both processes are important and the time-scale ratios offer an appropriate

---

[15]While, in a more sophisticated model, this may also drive an increase in magnetic energy density, the essential matter is to determine whether the additional contained CR energy density is enough to drive a wind. Whether the energy density is truly harboured in CRs, or has been transferred in part to the magnetic field to an equipartition level by some mechanism is incidental because the coupling between the CRs and magnetic field means they would essentially act together as a single fluid exerting an effective pressure gradient against gravity. It may therefore be useful to think of the CR pressure/energy densities mentioned here as the combined CR and magnetic pressures and energy densities.

[16]Note that equation (68) is identical to the expression given in Samui et al. (2010).

Table 2. Table to indicate the ability of systems to host a cold CR-driven outflow wind, choosing parameter values to favour the development of a wind. $v_{\mathrm{CR},\infty}$ is the terminal velocity of a wind, should one be able to form, calculated using equation (70) with the CR energy densities given in Table 1. f_{esc} gives the fraction of CRs expected to escape from the galaxy due to the action of the wind, estimated from the escape time-scale compared to the diffusion time-scale. Systems that are gravitationally bound when considering their mass against the energy density of CRs cannot develop a cold CR-driven outflow wind and no value is shown, although other driving mechanisms of outflows are still possible in which CRs may be advected (see Section 4.2.4) – e.g. thermal or line driven. Galactic size and total mass data used to calculate $v_{\mathrm{CR},\infty}$ for [1] Milky Way size (Xu et al. 2015); total mass (e.g. Kafle et al. 2014; McMillan 2017) [2] M31 size (Chapman et al. 2006); total mass (Kafle et al. 2018) [3] M82 size (see Davidge 2008 for discussion); total mass (e.g. Greve et al. 2002; Greco, Martini & Thompson 2012) [4] NGC 253 size and total mass (Bailin et al. 2011) [5] Arp 220 size and total mass (e.g. Scoville et al. 1991).

Source	$v_{\mathrm{CR},\infty}$ / km s^{-1}	f_{esc}/%
Milky Way [1]	–	–
M31 [2]	–	–
M82 [3]	700	92.7
NGC 253 [4]	570–670	95.0–95.7
Arp 220 [5]	< 130	< 33.4
Model: 0.1 SN yr^{-1}	–	–
Model: 1 SN yr^{-1}	–	–
Model: 10 SN yr^{-1}	390	49.8

scaling factor by which the CR containment level should be reduced to account for a non-negligible escaping fraction of particles, i.e. $f_{\mathrm{esc}} \approx \tau_{\mathrm{esc}}^{-1}/(\tau_{\mathrm{esc}}^{-1} + \tau_{\mathrm{diff}}^{-1})$, with $\tau_{\mathrm{esc}} \approx \ell_{\mathrm{gal}}/v_{\mathrm{CR},\infty}$ and $\tau_{\mathrm{diff}} \approx \ell_{\mathrm{gal}}^2/4D$.

Table 2 shows the terminal velocity $v_{\mathrm{CR},\infty}$ of cold CR-driven winds in various situations using the prescription described above. Note that there are cases where the CR-driven outflow condition cannot be satisfied. Of the models, only the most violently star-forming galaxy with the highest SN rate of 10 yr^{-1} is able to drive a wind to enable the leaking of CRs. In this case, the escape fraction of the CRs does not exceed 50 per cent. Our earlier results (in Section 4.1.4) omitting CR leaking are therefore not substantially different to those taking full account of CR leaking. However, based on the level of CR heating in the system investigated in Section 4.1.4 (whether or not accounting for CR escape), we may conclude that CRs could be advected by a thermally driven outflow (see Section 4.2.4) shortly after the onset of starburst activity. The advection of CRs by such a wind and the consequences of this process will be discussed in Owen et al. (2018).

4.2.4 Dilution by advective transport

As per the empirical scaling outlined in Section 3.3.2, the value of the diffusion coefficient is about 3×10^{28} cm^2 s^{-1} for a 1 GeV CR when the magnetic field has reached saturation. With the length-scale of the system $\ell \approx 1$ kpc, we can estimate the CR diffusion time-scale as

$$\tau_{\mathrm{diff}} \approx \frac{\ell^2}{4D} \approx 2.5\,\mathrm{Myr} \,. \tag{71}$$

Protogalaxies with strong star-formation activities are expected to exhibit wind outflows. These outflows carry CRs trapped by magnetic fields in the wind away from the host galaxy, thus reducing the amount of CR energy available for heating the ISM. The winds and outflows in nearby starburst galaxies generally have bulk outflow velocities v of around 10^2–10^3 km s^{-1} (see Chevalier & Clegg
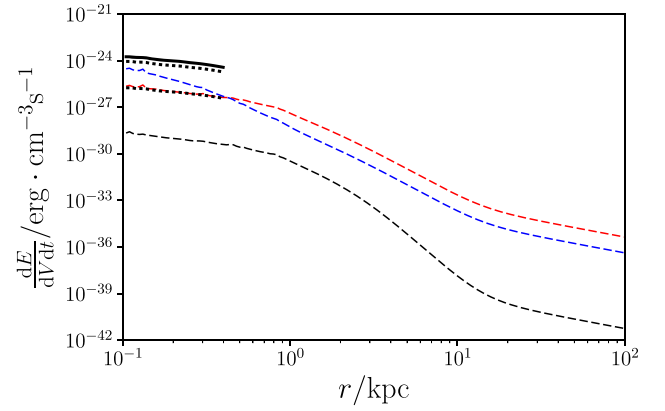
Figure 8. Steady-state CR heating profiles for the case with 10, 50, and 99 per cent of the particles are removed by advection (solid line, upper dotted line, and lower dotted line in black, respectively). Heating profiles corresponding to starlight, X-rays, and free-streaming CRs before magnetic containment occurs are also shown (dashed lines in blue, red, and black, respectively) for comparison. The other parameters are the same as those of the corresponding cases shown in Fig. 6. All lines are calculated for $\mathcal{R}_{\mathrm{SN}} = 1.0$ yr^{-1}, corresponding to a star-formation rate of around 160 M$_\odot$ yr^{-1} by the relation $\mathcal{R}_{\mathrm{SF}} \approx 160\,\mathrm{M}_\odot$ yr$^{-1}(\mathcal{R}_{\mathrm{SN}}/\mathrm{yr}^{-1})$ (see Section 3.3.1).

1985; Seaquist, Bell & Bignell 1985) and the corresponding advection time-scale of CR transport is

$$\tau_{\mathrm{adv}} \approx \frac{\ell}{v} \approx (1-10)\mathrm{Myr} \,. \tag{72}$$

Given that the time-scales of advection and diffusion are similar, these processes must be comparably important in governing CR propagation (and hence the energy budget) in ISM heating. The results shown in Fig. 6 and Table 1 are obtained without the inclusion of advective transport of CRs. If a substantial fraction of CRs are carried away in advection by galactic outflows, the CR heating of ISM will be reduced accordingly. Large-scale wind outflows in nearby starburst galaxies generally have a wide-angle cone morphology, with the star formation in the galactic disc below the cone providing the power. While advection is expected to dominate the CR transport process in the wind, one would expect the heating of the ISM to be caused by the CRs diffusing across the galactic disc. Thus, to have a rough estimate of how much advective transport is required to quench CR heating, we may consider a simple prescription of removing a specific fraction of the CRs produced in the SN events, attributing their loss to advective transport out of the environment. In Fig. 8 we show the steady-state heating rate for 10, 50, and 99 per cent of the CRs being removed (presumably) by the advective process (at SN event rate of $\mathcal{R}_{\mathrm{SN}} = 1.0$ yr^{-1}). We conclude that even when 99 per cent of the CRs are advected out of the system, CR heating (which remains at least comparable with starlight and X-ray heating) cannot be neglected when modelling the thermodynamics of the ISM in protogalaxies.

5 DISCUSSIONS AND CONCLUSIONS

5.1 Astrophysical implications

In this study we have demonstrated that CR heating power can exceed that due to conventional radiative heating provided by starlight and diffuse X-rays for conditions appropriate to protogalaxies exhibiting strong star-formation activity. This enhanced heating by CRs yields hotter proto-stellar gas, while CR scattering and

interactions will induce additional turbulence throughout the ISM of the host (see e.g. Niemiec et al. 2008; Bykov, Osipov & Ellison 2011; Rogachevskii et al. 2012). The resulting additional (thermal and turbulent) pressure support will lead to increased Jeans masses in star-forming regions (see e.g. Papadopoulos et al. 2011; Papadopoulos, Thi & Reimer 2013), with proto-stars pushed to higher initial masses (see discussions in Kuwabara & Ko 2006; Ko & Lo 2009; Hanawa & Tomisaka 2015a, 2015b; Kuwabara & Ko 2015).

There are also suggestions that severe CR heating can quench star-formation entirely in host environments, perhaps even evaporating star-forming regions altogether in the most extreme cases (Guo & Oh 2008; Gabor et al. 2011). Indeed, CRs may heat proto-stellar clumps throughout the host galaxy more effectively than radiation due to higher levels of energy deposition at the point of interaction and the possibility that they may be guided into star-forming regions by the threading magnetic fields (see e.g. Jokipii 1966; Ferland 2009). In comparison with sub-keV X-rays and ultraviolet radiation, CRs are also less prone to shielding by the neutral material present in stellar nurseries and collapsing clouds and cores.

Increased containment of CRs within the host galaxy would be expected to increase the rate of pp-interactions driving the emission of γ-rays (Abdo et al. 2010; Wang & Fields 2014, 2018; Yoast-Hull et al. 2016), which is expected to be coupled with the CR heating effect (see Section 2 for details). This may also be the case for synchrotron emission following an enhanced number density of high-energy CR secondary electrons injected into dense regions of the environment by the primary CR proton interactions. These secondaries may then interact with the strengthening galactic magnetic field (see e.g. Schleicher & Beck 2013) and lose energy by synchrotron emission. At high redshift, the scattering of these energetic CR electrons off CMB photons is also likely to drive a level of X-ray emission. The resulting X-ray illumination in high redshift starbursts was first introduced in Schober, Schleicher & Klessen (2015); see also Schleicher & Beck (2013).

On larger scales in the environment outside the host galaxy, the CR containment and the subsequent release of the CR energy may drive large-scale galactic outflows and fountains (Shapiro & Field 1976; Bregman 1980; Heesen et al. 2016). These outflows, in turn, may act as vehicles by which CRs are delivered into the circumgalactic medium and beyond into intergalactic space (Heesen et al. 2016). This process may be a possible candidate for the pre-heating of the IGM in advance of cosmic reionization (Sazonov & Sunyaev 2015; Leite et al. 2017) at least in the proximity to a conglomeration of galaxies exhibiting violent star-forming activity. Additionally, the radiative emission from a host galaxy due to the contained CRs – in particular the X-ray emission resulting from inverse-Compton scattering of electrons (Schober et al. 2015) – could begin to drive heating in the ISM of nearby neighbouring galaxies, possibly impacting on their own internal processes via X-ray heating.

5.2 Remarks

Observations, via Zeeman effect measurements (see e.g. Bergin & Tafalla 2007; Koch et al. 2015; Ching et al. 2017) and dust emission polarimetry (e.g. see Planck Collaboration XXXV 2016a), have revealed complex magnetic structures in the Galactic ISM. The alignment and the spatial structure of magnetic fields in and around dense and/or star-forming regions have shown great diversity and also vary over different length scales in the same system (see Rao et al. 2009; Alves et al. 2011; Chen et al. 2012; Wang et al. 2015; Hull et al. 2017). In the densest parts of some molecular clouds,

where stars are spawned, the local magnetic field can reach levels of ~1 mG (Crutcher et al. 2010). Such field strengths are strong enough to influence the propagation of CRs with energies even above a GeV, which will have gyration radii ~10^{11} cm (note that lower-energy MeV CRs will have smaller-scale gyration radii). The interaction of CRs with strong localized magnetic fields therefore needs to be modelled more thoroughly so as to determine their effects on CR scattering and propagation, and how the energy-selected CR containment by such localized magnetic fields can impact on both the local and global thermodynamics of the ISM of protogalactic environments.

We have also examined the relative effect of starlight and X-ray heating. While intended as a comparison to the CR heating, there is an intriguing interplay between the different processes in addition to their relative importance in the thermodynamic context. For instance, the Compton scattering between the starlight photons with the high-energy electrons that are produced by the interactions of the CR protons may increase the level of X-rays inferred by stellar source counts, e.g. for SN remnants, X-ray binaries, or colliding winds in stars. This effect may be particularly prevalent for violent star-forming protogalaxies at high redshifts and may considerably enhance the 'indirect' CR heating impact on the interior and surrounding environment of the host.

We have employed a simple parametric model as a demonstration of the importance of CR heating via hadronic processes in a protogalaxy. One of the crucial parameters in the model is the SN event rate, which determines the total power available for the CR heating process, be they confined or free-streaming. A uniform SN event rate is adopted in this study. The SN rate and magnetic fields are expected to co-evolve together if galactic scale magnetism in the protogalaxy is seeded by SN events. In this coevolution scenario, the containment of CRs in the initial and transient stage would be significantly different. However, one would not expect a substantial qualitative difference between including and excluding such effect once the magnetic field evolution has saturated. Although we have assumed a uniform SN event rate, the results obtained as such are nevertheless reasonable estimates.

5.3 Conclusions

In this study we have shown that the containment of CRs by a developing protogalactic magnetic field can arise within 10 Myr if employing an SN turbulent-dynamo driven model as outlined in Schober et al. (2013). Before this time, there is a window during which CRs may freely stream out of their host and into their surrounding environment. In the case of a protogalaxy actively forming stars at a rate of around ~$160 \, M_\odot \, yr^{-1}$ (leading to SN event rate of ~$1.0 \, yr^{-1}$), the calculated containment amplifies the expected ISM heating effect due to the CRs from a level of around 10^{-29} erg cm^{-3} s^{-1} (which is lower than the conventional radiative heating mechanisms by stellar emission and X-rays) to around 10^{-24} erg cm^{-3}s^{-1}. Extrapolated from this level of CR heating within the central region of the protogalaxy, an extra-galactic heating rate of ~10^{-37} erg cm^{-3}s^{-1} at around 10 kpc from the the protogalaxy, and ~10^{-41} erg cm^{-3}s^{-1} at 100 kpc from the protogalaxy is also expected.

The level of CR heating in the protogalactic environment obtained here also implies that CR heating in the IGM in the vicinity may also be non-negligible. This opens up many new questions about the impacts such an effect may have, and the degree to which it could be maintained.

REFERENCES

Abbasi R. U. et al., 2010, Phys. Rev. Lett., 104, 161101
Abdo A. A. et al., 2010, A&A, 523, L2
Abe F. et al., 1990, Phys. Rev. D, 41, 2330
Adams S. M., Kochanek C. S., Beacom J. F., Vagins M. R., Stanek K. Z., 2013, ApJ, 778, 164
Adebahr B., Krause M., Klein U., Weżgowiec M., Bomans D. J., Dettmar R. J., 2013, A&A, 555, A23
Adrián-Martínez S. et al., 2016, Phys. Lett. B, 760, 143
Aharonian F. A., Atoyan A. M., 2000, A&A, 362, 937
Aharonian F., Bykov A., Parizot E., Ptuskin V., Watson A., 2012, Space Sci. Rev., 166, 97
Albajar C. et al., 1990, Nucl. Phys. B, 335, 261
Albini E., Capiluppi P., Giacomelli G., Rossi A. M., 1976, Nuovo Cimento A Ser., 32, 101
Alexopoulos T. et al., 1998, Phys. Lett. B, 435, 453
Allard D., Parizot E., Olinto A., 2007, Astropart. Phys., 27, 61
Almeida S. P. et al., 1968, Phys. Rev., 174, 1638
Alner G. J. et al., 1984, Phys. Lett. B, 138, 304
Alner G. J. et al., 1985, Phys. Lett. B, 160, 193
Alves F. O., Girart J. M., Lai S.-P., Rao R., Zhang Q., 2011, ApJ, 726, 63
Amenomori M. et al., 2008, ApJ, 672, L53
Ansorge R. E. et al., 1989, Z. Phys., C43, 357
Appleton P. N. et al., 2015, ApJ, 812, 118
Arnison G. et al., 1983, Phys. Lett. B, 123, 108
Atoyan A. M., Dermer C. D., 2003, ApJ, 586, 79
Badenes C., Maoz D., Draine B. T., 2010, MNRAS, 407, 1301
Baek C. H., Kang H., Kim J., Ryu D., 2005, ApJ, 630, 689
Bailin J., Bell E. F., Chappell S. N., Radburn-Smith D. J., de Jong R. S., 2011, ApJ, 736, 24
Bakes E. L. O., Tielens A. G. G. M., 1994, ApJ, 427, 822
Baldini A., Flaminio V., Moorhead W., Morrison D., 1987, Total Cross-Sections for Reactions of High Energy Particles. Landolt-Börnstein: Numerical Data and Functional Relationships in Science and Technology - New Series / Elementary Particles, Nuclei and Atoms. Springer, Dordrecht, the Netherlands
Balsara D. S., Kim J., Low M.-M. M., Mathews G. J., 2004, ApJ, 617, 339
Barger A. J. et al., 2014, ApJ, 784, 9
Bartos I., Marka S., 2015, preprint (arXiv:1509.00983)
Beck R., Wielebinski R., 2013, Magnetic Fields in Galaxies. Springer, Dordrecht, the Netherlands, p. 641
Beck R. Fletcher A. Shukurov A. Snodin A. Sokoloff D. D. Ehle M. s D. Mo Shoutenkov V., 2005, A&A, 444, 739

Beck A. M., Lesch H., Dolag K., Kotarba H., Geng A., Stasyszyn F. A., 2012, MNRAS, 422, 2152
Becker J. K., 2008, Phys. Rep., 458, 173
Beech M., 2011, JRASC, 105, 232
Beelen A., Cox P., Benford D. J., Dowell C. D., Kovács A., Bertoldi F., Omont A., Carilli C. L., 2006, ApJ, 642, 694
Bell A. R., 1978, MNRAS, 182, 147
Bell A. R., 2013, Astropart. Phys., 43, 56
Bell A. R., Schure K. M., Reville B., Giacinti G., 2013, MNRAS, 431, 415
Benhabiles-Mezhoud H., Kiener J., Tatischeff V., Strong A. W., 2013, ApJ, 763, 98
Berezhko E. G., Ellison D. C., 1999, ApJ, 526, 385
Berezinskii V. S., Bulanov S. V., Dogiel V. A., Ptuskin V. S., 1990, Astrophysics of Cosmic Rays. North-Holland, Amsterdam
Berezinsky V. S., Gazizov A. Z., 1993, Phys. Rev. D, 47, 4206
Berezinsky V. S., Grigor'eva S. I., 1988, A&A, 199, 1
Berezinsky V., Gazizov A., Grigorieva S., 2006, Phys. Rev. D, 74, 043005
Bergin E. A., Tafalla M., 2007, ARA&A, 45, 339
Bernet M. L., Miniati F., Lilly S. J., Kronberg P. P., Dessauges-Zavadsky M., 2008, Nature, 454, 302
Bethe H., Heitler W., 1934, Proc. R. Soc. A, 146, 83
Bethe H. A., Maximon L. C., 1954, Phys. Rev., 93, 768
Bianchi S., Schneider R., 2007, MNRAS, 378, 973
Blasi P., 2011, in Giani S., Leroy C., Rancoita P. G., eds, Cosmic Rays for Particle and Astroparticle Physics, p. 493
Blasi P., 2014, Comptes Rendus Phys., 15, 329
Blattnig S. R., Swaminathan S. R., Kruger A. T., Ngom M., Norbury J. W., 2000, Phys. Rev. D, 62, 094030
Blumenthal G. R., 1970, Phys. Rev. D, 1, 1596
Bocchio M., Marassi S., Schneider R., Bianchi S., Limongi M., Chieffi A., 2016, A&A, 587, A157
Bouwens R. J. et al., 2016, ApJ, 833, 72
Braginskii S. I., 1965, Rev. Plasma Phys., 1, 205
Breakstone A. et al., 1984, Phys. Rev. D, 30, 528
Bregman J. N., 1980, ApJ, 236, 577
Breitschwerdt D., McKenzie J. F., Voelk H. J., 1991, A&A, 245, 79
Brunetti G., Jones T. W., 2014, IJMPD, 23, 1430007
Burton M. G., Hollenbach D. J., Tielens A. G. G. M., 1990, ApJ, 365, 620
Bykov A. M., Osipov S. M., Ellison D. C., 2011, MNRAS, 410, 39
Capak P. L. et al., 2015, Nature, 522, 455
Caprioli D., 2012, J. Cosmol. Astropart. Phys., 7, 038
Chapman S. C., Ibata R., Lewis G. F., Ferguson A. M. N., Irwin M., McConnachie A., Tanvir N., 2006, ApJ, 653, 255
Chen W. P., Su B. H., Eswaraiah C., Pandey A. K., Wang C. W., Lai S. P., Tamura M., Sato S., 2012, Proc. IAU Symp. 10, Cambridge Univ. Press, Cambridge, p. 390
Chen J., Bryan G. L., Salem M., 2016, MNRAS, 460, 3335
Chevalier R. A., Clegg A. W., 1985, Nature, 317, 44
Ching T.-C., Lai S.-P., Zhang Q., Girart J. M., Qiu K., Liu H. B., 2017, ApJ, 838, 121
Cruddace R., Paresce F., Bowyer S., Lampton M., 1974, ApJ, 187, 497
Crutcher R. M., Wandelt B., Heiles C., Falgarone E., Troland T. H., 2010, ApJ, 725, 466
Dar A., de Rújula A., 2008, Phys. Rep., 466, 179
Davidge T. J., 2008, AJ, 136, 2502
Dehnen W., 1993, MNRAS, 265, 250
Dermer C. D., Menon G., 2009, High Energy Radiation from Black Holes: Gamma Rays Cosmic Rays, and Neutrinos. Princeton series in astrophysics, Princeton Univ. Press, Princeton, NJ
Dermer C. D., Powale G., 2013, A&A, 553, A34
Dermer C. D., Schlickeiser R., 1991, A&A, 252, 414
Di Fazio A., Occhionero F., Vagnetti F., 1979, A&A, 72, 204
Díaz-Rodríguez M., Murphy J. W., Rubin D. A., Dolphin A. E., Williams B. F., Dalcanton J. J., 2018, ApJ, 861, 92
Diehl R. et al., 2006, Nature, 439, 45
Dragicevich P. M., Blair D. G., Burman R. R., 1999, MNRAS, 302, 693
Draine B. T., 1978, ApJS, 36, 595

Draine B. T., 2011, Physics of the Interstellar and Intergalactic Medium, Princeton University Press, Princeton, NJ

Drury L. O., Falle S. A. E. G., 1986, MNRAS, 223, 353

Federrath C., Chabrier G., Schober J., Banerjee R., Klessen R. S., Schleicher D. R. G., 2011, Phys. Rev. Lett., 107, 114504

Fenech D., Beswick R., Muxlow T. W. B., Pedlar A., Argo M. K., 2010, MNRAS, 408, 607

Ferland G. J., 2009, in Strassmeier K. G., Kosovichev A. G., Beckman J. E., eds, IAU Symp. 259, Cosmic Magnetic Fields: From Planets, to Stars and Galaxies, Kluwer, Dordrecht, p. 25

Fermi E., 1949, Phys. Rev., 75, 1169

Ferrara A., Viti S., Ceccarelli C., 2016, MNRAS, 463, L112

Ferriere K. M., 2001, Rev. Mod. Phys., 73, 1031

Fields B. D., Olive K. A., Cassé M., Vangioni-Flam E., 2001, A&A, 370, 623

Fiete Grosse-Oetringhaus J., Reygers K., 2010, J. Phys. G Nucl. Phys., 37, 083001

Fletcher A., Beck R., Shukurov A., Berkhuijsen E. M., Horellou C., 2011, MNRAS, 412, 2396

Fryer C. L., 1999, ApJ, 522, 413

Gabor J. M., Dave R., Oppenheimer B. D., Finlator K., 2011, MNRAS, 417, 2676

Gaggero D., 2012, Cosmic Ray Diffusion in the Galaxy and Diffuse Gamma Emission. Springer Theses, Springer, Berlin, Heidelberg

Gall C., Hjorth J., Andersen A. C., 2011, ARA&A, 19, 43

Gao J., Jiang B. W., Li A., Li J., Wang X., 2015, ApJ, 807, L26

Giammanco C., Beckman J. E., 2005, A&A, 437, L11

Ginolfi M., Graziani L., Schneider R., Marassi S., Valiante R., Dell'Agli F., Ventura P., Hunt L. K., 2018, MNRAS, 473, 4538

Ginzburg V. L., 1996, Phys. Uspekhi, 39, 155

Glover S. C. O., Clark P. C., 2012, MNRAS, 421, 9

González-López J. et al., 2014, ApJ, 784, 99

Gould R. J., 1975, ApJ, 196, 689

Gould R. J., Burbidge G. R., 1965, Ann. Astrophys., 28, 171

Greco J. P., Martini P., Thompson T. A., 2012, ApJ, 757, 24

Greisen K., 1966, Phys. Rev. Lett., 16, 748

Greve A., Wills K. A., Neininger N., Pedlar A., 2002, A&A, 383, 56

Guo F., Oh S. P., 2008, MNRAS, 384, 251

H.E.S.S. Collaboration, 2018, A&A, 612, A9

Hakobyan A. A. et al., 2011, Astrophysics, 54, 301

Hammond A. M., Robishaw T., Gaensler B. M., 2012, preprint (arXiv: 1209.1438)

Hanawa T., Tomisaka K., 2015a, ApJ, 801, 11

Hanawa T., Tomisakar K., 2015b, Proc. IAU Symp. 11, Structure and Stability of Filamentary Clouds Supported by Lateral Magnetic Field, Cambridge Univ. Press, Cambridge,

Heesen V., Dettmar R.-J., Krause M., Beck R., Stein Y., 2016, MNRAS, 458, 332

Heger A., Fryer C. L., Woosley S. E., Langer N., Hartmann D. H., 2003, ApJ, 591, 288

Hernquist L., Springel V., 2003, MNRAS, 341, 1253

Hillas A. M., 1984, ARA&A, 22, 425

Hirashita H., Buat V., Inoue A. K., 2003, A&A, 410, 83

Howard A. M., Kulsrud R. M., 1997, ApJ, 483, 648

Hu C.-Y., Naab T., Glover S. C. O., Walch S., Clark P. C., 2017, MNRAS, 471, 2151

Hull C. L. H. et al., 2017, ApJ, 842, L9

Hümmer S., Rüger M., Spanier F., Winter W., 2010, ApJ, 721, 630

Hutton S., Ferreras I., Wu K., Kuin P., Breeveld A., Yershov V., Cropper M., Page M., 2014, MNRAS, 440, 150

Hutton S., Ferreras I., Yershov V., 2015, MNRAS, 452, 1412

Ipavich F. M., 1975, ApJ, 196, 107

Iwamoto K., Kunugise T., 2006, AIP Conf. Proc., 847, 406

Janka H.-T., 2012, Annu. Rev. Nucl. Part. Sci., 62, 407

Jennings Z. G., Williams B. F., Murphy J. W., Dalcanton J. J., Gilbert K. M., Dolphin A. E., Weisz D. R., Fouesneau M., 2014, ApJ, 795, 170

Jokipii J. R., 1966, ApJ, 146, 480

Jost R., Luttinger J. M., Slotnick M., 1950, Phys. Rev., 80, 189

Kafexhiu E., Aharonian F., Taylor A. M., Vila G. S., 2014, Phys. Rev. D, 90, 123014

Kafle P. R., Sharma S., Lewis G. F., Bland-Hawthorn J., 2014, ApJ, 794, 59

Kafle P. R., Sharma S., Lewis G. F., Robotham A. S. G., Driver S. P., 2018, MNRAS, 475, 4043

Karlsson N., 2008, AIP Conf. Proc., 1085, 561

Kazantsev A. P., 1968, JETP, 26, 1031

Klein S. R., 2006, Radiat. Phys. Chem., 75, 696

Knudsen K. K., Richard J., Kneib J.-P., Jauzac M., Clement B., Drouart G., Egami E., Lindroos L., 2016, MNRAS, 462, L6

Kobzar O., Sushchov O., Hnatyk B., Marchenko V., 2016, preprint (arXiv: 1602.01683)

Koch P.M. et al., 2015, EAS Publ. Ser., 75, 159

Ko C.-M., Lo Y.-Y., 2009, ApJ, 691, 1587

Kolmogorov A., 1941, Akademiia Nauk SSSR Doklady, 30, 301

Kotera K., Olinto A. V., 2011, ARA&A, 49, 119

Kotera K., Allard D., Olinto A. V., 2010, J. Cosmol. Astropart. Phys., 10, 013

Kulsrud R. M., 2005, Plasma Physics for Astrophysics, Princeton University Press, Princeton, NJ

Kuwabara T., Ko C.-M., 2006, ApJ, 636, 290

Kuwabara T., Ko C.-M., 2015, ApJ, 798, 79

Lacki B. C., Beck R., 2013, MNRAS, 430, 3171

Lacki B. C., Thompson T. A., 2012, AIP Conf. Proc., 1505, 56

Lacki B. C., Thompson T. A., Quataert E., Loeb A., Waxman E., 2011, ApJ, 734, 107

Lada C. J., 2006, ApJ, 640, L63

Latif M. A., Schleicher D. R. G., Schmidt W., Niemeyer J., 2013, MNRAS, 432, 668

Ledrew G., 2001, JRASC, 95, 32

Leite N., Evoli C., D'Angelo M., Ciardi B., Sigl G., Ferrara A., 2017, MNRAS, 469, 416

Leitherer C. et al., 1999, ApJS, 123, 3

Lemoine-Goumard M., Renaud M., Vink J., Allen G. E., Bamba A., Giordano F., Uchiyama Y., 2012, A&A, 545, A28

Lenc E., Tingay S. J., 2006, AJ, 132, 1333

Li J.-T., Wang Q. D., 2013, MNRAS, 435, 3071

Loeb A., Waxman E., 2006, J. Cosmol. Astropart. Phys., 5, 003

Lonsdale C. J., Diamond P. J., Thrall H., Smith H. E., Lonsdale C. J., 2006, ApJ, 647, 185

Maiolino R. et al., 2015, MNRAS, 452, 54

McCray R., Buff J., 1972, ApJ, 175, L65

McMillan P. J., 2017, MNRAS, 465, 76

Meijerink R., Spaans M., 2005, A&A, 436, 397

Michałowski M. J., Murphy E. J., Hjorth J., Watson D., Gall C., Dunlop J. S., 2010, A&A, 522, A15

Morlino G., Caprioli D., 2012, A&A, 538, A81

Mosleh M. et al., 2012, ApJ, 756, L12

Mücke A., Rachen J. P., Engel R., Protheroe R. J., Stanev T., 1999, PASA, 16, 160

Muno M. P. et al., 2006, ApJ, 636, L41

Nakamura K., 2010, J. Phys. G Nucl. Part. Phys., 37, 075021

Nath B. B., Biermann P. L., 1993, MNRAS, 265, 421

Nath B. B., Laskar T., Shull J. M., 2008, ApJ, 682, 1055

Niemiec J., Pohl M., Stroman T., Nishikawa K.-I., 2008, ApJ, 684, 1174

Nozawa T., Kozasa T., Habe A., Dwek E., Umeda H., Tominaga N., Maeda K., Nomoto K., 2007, ApJ, 666, 955

Ono Y. et al., 2013, ApJ, 777, 155

Ota K. et al., 2014, ApJ, 792, 34

Ouchi M. et al., 2013, ApJ, 778, 102

Owen E. R., Wu K., Surajbali P., Jacobsen I. B., 2017, preprint (arXiv: 1708.06808)

Owen E. R., Jin X., Wu K., Chan S., 2018, submitted

Papadopoulos P. P., Thi W.-F., Miniati F., Viti S., 2011, MNRAS, 414, 1705

Papadopoulos P. P., Thi W.-F., Reimer O., 2013, The Initial Conditions of Star Formation: Cosmic Rays as the Fundamental Regulators. Springer, Berlin, Heidelberg, p. 41

Patrignani C. et al., 2016, Chin. Phys., C40, 100001

Pfrommer C., Springel V., Jubelgas M., Ensslin T. A., 2007, in Metcalfe N., Shanks T., eds, ASP Conf. Ser. Vol. 379, Cosmic Frontiers. Astron. Soc. Pac., San Francisco, p. 221

Planck Collaboration XXXV, 2016a, A&A, 586, A138

Planck Collaboration XIII, 2016b, A&A, 594, A13

Pollack J. B., Fazio G. G., 1963, Phys. Rev., 131, 2684

Protheroe R. J., Johnson P. A., 1996, Astropart. Phys., 4, 253

Pudritz R., Fich M., 2012, Galactic and Extragalactic Star Formation. Nato Science Series C. Springer, the Netherlands

Rao R., Girart J. M., Marrone D. P., Lai S.-P., Schnee S., 2009, ApJ, 707, 921

Recchia S., Blasi P., Morlino G., 2016, MNRAS, 462, 4227

Rees M. J., 1987, QJRAS, 28, 197

Riechers D. A. et al., 2014, ApJ, 796, 84

Rieder M., Teyssier R., 2016, MNRAS, 457, 1722

Rimondi F., 1993, in 23rd International Symposium on Ultra-High Energy Multiparticle Phenomena Aspen, Colorado, September 12–17, 1993. p. 0400. http://lss.fnal.gov/cgi-bin/find_paper.pl?conf-93-359

Robertson B. E., Ellis R. S., Dunlop J. S., McLure R. J., Stark D. P., 2010, Nature, 468, 49

Rogachevskii I., Kleeorin N., Brandenburg A., Eichler D., 2012, ApJ, 753, 6

Rybicki G. B., Lightman A. P., 1986, Radiative Processes in Astrophysics. Wiley, New York

Salem M., Bryan G. L., 2014, MNRAS, 437, 3312

Samui S., Subramanian K., Srianand R., 2010, MNRAS, 402, 2778

Sarkar K. C., Nath B. B., Sharma P., Shchekinov Y., 2016, ApJ, 818, L24

Sazonov S., Sunyaev R., 2015, MNRAS, 454, 3464

Schleicher D. R. G., Beck R., 2013, A&A, 556, A142

Schober J., Schleicher D. R. G., Klessen R. S., 2013, A&A, 560, A87

Schober J., Schleicher D. R. G., Klessen R. S., 2015, MNRAS, 446, 2

Schure K. M., Bell A. R., 2013, MNRAS, 435, 1174

Scoville N. Z., Sargent A. I., Sanders D. B., Soifer B. T., 1991, ApJ, 366, L5

Seaquist E. R., Bell M. B., Bignell R. C., 1985, ApJ, 294, 546

Serra P., Doré O., Lagache G., 2016, ApJ, 833, 153

Shapiro P. R., Field G. B., 1976, ApJ, 205, 762

Sigl G., Olinto A. V., Jedamzik K., 1997, Phys. Rev. D, 55, 4582

Silvia D. W., Smith B. D., Shull J. M., 2010, ApJ, 715, 1575

Skorodko T. et al., 2008, Eur. Phys. J. A, 35, 317

Slattery P., 1972, Phys. Rev. Lett., 29, 1624

Smartt S. J., 2009, ARA&A, 47, 63

Smartt S. J., Eldridge J. J., Crockett R. M., Maund J. R., 2009, MNRAS, 395, 1409

Smith N., Vink J. S., de Koter A., 2004, ApJ, 615, 475

Smith N., Hinkle K. H., Ryde N., 2009, AJ, 137, 3558

Smith N., Li W., Filippenko A. V., Chornock R., 2011, MNRAS, 412, 1522

Socrates A., Davis S. W., Ramirez-Ruiz E., 2008, ApJ, 687, 202

Solomon P. M., Vanden Bout P. A., 2005, ARA&A, 43, 677

Stark D. P., Schenker M. A., Ellis R., Robertson B., McLure R., Dunlop J., 2013, ApJ, 763, 129

Stecker F. W., Tsuruta S., Fazio G. G., 1968, ApJ, 151, 881

Stecker F. W., Malkan M. A., Scully S. T., 2006, ApJ, 648, 774

Stepney S., Guilbert P. W., 1983, MNRAS, 204, 1269

Strong A. W., Porter T. A., Digel S. W., Jóhannesson G., Martin P., Moskalenko I. V., Murphy E. J., Orlando E., 2010, ApJ, 722, L58

Sur S., Bhat P., Subramanian K., 2018, MNRAS, 475, L72

The HSC Collaboration, 2012, Observational Survey Proposal, Wide-field Imaging with Hyper Suprime-Cam: Cosmology and Galaxy Evolution. A Strategic Survey Proposal for the Subaru Telescope. NAOJ

Thome W. et al., 1977, Nucl. Phys., B129, 365

Thompson T. A., Quataert E., Waxman E., 2007, ApJ, 654, 219

Tominaga N. et al., 2008, ApJ, 687, 1208

Tremaine S., Richstone D. O., Byun Y.-I., Dressler A., Faber S. M., Grillmair C., Kormendy J., Lauer T. R., 1994, AJ, 107, 634

Tueros M., del Valle M. V., Romero G. E., 2014, A&A, 570, L3

Valdés M., Evoli C., Ferrara A., 2010, MNRAS, 404, 1569

Walch S., Naab T., 2015, MNRAS, 451, 2757

Walker M. A., 2016, ApJ, 818, 23

Walter F. et al., 2012, ApJ, 752, 93

Wang X., Fields B. D., 2014, AIP Conf. Proc., 1595, 231

Wang X., Fields B. D., 2018, MNRAS, 474, 4073

Wang C.-H., 1991, PhD thesis, Iowa State Univ.

Wang J.-W., Eswaraiah C., Lai S.-P., Clemens D. P., Chen W.-P., Pandey A. K., 2015, Proc. IAU, 11

Watson M. G., Stanger V., Griffiths R. E., 1984, ApJ, 286, 144

Weiner B. J. et al., 2009, ApJ, 692, 187

Whalen D. J., Johnson J. L., Smidt J., Meiksin A., Heger A., Even W., Fryer C. L., 2013, ApJ, 774, 64

Whitmore J., 1974, Phys. Rep., 10, 273

Wolfire M. G., Hollenbach D., McKee C. F., Tielens A. G. G. M., Bakes E. L. O., 1995, ApJ, 443, 152

Wright W. P., Kneller J. P., Ohlmann S. T., Röpke F. K., Scholberg K., Seitenzahl I. R., 2017, Phys. Rev. D, 95, 043006

Xu Y., Newberg H. J., Carlin J. L., Liu C., Deng L., Li J., Schonrich R., Yanny B., 2015, ApJ, 801, 105

Yamasawa D., Habe A., Kozasa T., Nozawa T., Hirashita H., Umeda H., Nomoto K., 2011, ApJ, 735, 44

Yoast-Hull T. M., Gallagher J. S., III, Zweibel E. G., 2016, MNRAS, 457, L29

Zatsepin G. T., Kuz'min V. A., 1966, JETPL, 4, 78

APPENDIX A: ENERGY DENSITY OF SPATIALLY EXTENDED SOURCES

To extend the model radiation field from a single point source to an ensemble of N sources, we introduce a distribution function $f(r)$ for the sources in a sphere. The effective distance between the nearest source and some observer located within the spherical distribution is $\tilde{r}$. In an axisymmetric system, the minimum distance to a source from a randomly positioned observer is $\tilde{r}$ while the maximum distance is the radius of the extended source, r_{sph}, with the average energy density due to the radiation from the entire distribution of sources in the ensemble as

$$
\begin{aligned}
U &= \frac{L}{4\pi c} \int_{\tilde{r}}^{r_{\mathrm{sph}}} \mathrm{d}r \, 4\pi r^2 \frac{f(r)}{r^2} \\
&= \frac{L}{c} \int_{\tilde{r}}^{r_{\mathrm{sph}}} \mathrm{d}r \, f(r)
\end{aligned} \tag{A1}
$$

where the distribution function $f(r)$ for a uniform distribution of sources is

$$
f(r) = \frac{3}{4\pi} N \left(r_{\mathrm{gal}}^3 - \tilde{r}^3 \right) . \tag{A2}
$$

This yields

$$
\begin{aligned}
U &= \frac{3}{4\pi} \frac{L}{c} N \left(\frac{r_{\mathrm{sph}} - \tilde{r}}{r_{\mathrm{sph}}^3 - \tilde{r}^3} \right) \\
&= \frac{3}{4\pi} N r_{\mathrm{sph}}^2 \left[1 + \left(\frac{\tilde{r}}{r_{\mathrm{sph}}} \right) + \left(\frac{\tilde{r}}{r_{\mathrm{sph}}} \right)^2 \right]^{-1} .
\end{aligned} \tag{A3}
$$

The number of sources within the ensemble can be calculated by the ratio of volume taken up by the source (based on the nearest distance from the observer) to the size of the ensemble,

$$
N = \frac{4\pi r_{\mathrm{sph}}^3}{4\pi \tilde{r}^3} = \left(\frac{r_{\mathrm{sph}}}{\tilde{r}} \right)^3 \tag{A4}
$$

which implies

$$
\frac{\tilde{r}}{r_{\mathrm{gal}}} = \left(\frac{1}{N} \right)^{1/3} . \tag{A5}
$$

Then, substitution of A5 into equation (A3) gives

$$U = \frac{3}{4\pi} \frac{L}{c} \frac{N}{r_{sph}^2} \left[1 + \left(\frac{1}{N}\right)^{1/3} + \left(\frac{1}{N}\right)^{2/3} \right]^{-1} . \tag{A6}$$

In the limit of $N \to 1$, the usual inverse-square law result for radiation can be recovered, i.e. $U = L/4\pi c r_{sph}^2$. For large N, the result becomes

$$U \to \frac{LN}{4\pi c} \left(\frac{3}{r_{sph}^2} \right) . \tag{A7}$$

Comparison with an MC approach confirms the analytical result above for the energy density at randomly selected points in a spherical distribution of N sources. Division of equation (A6) by the typical photon energy of $2.82\,k_B T_* \approx 3\,k_B T_*$ yields an estimate for the photon number density of the radiation field in the case of stars distributed in a galaxy as

$$n_{ph} \approx \frac{3}{12\pi k_B T_*} \frac{L}{c} \frac{N}{r_{gal}^2} \left[1 + \left(\frac{1}{N}\right)^{1/3} + \left(\frac{1}{N}\right)^{2/3} \right]^{-1} . \tag{A8}$$

APPENDIX B: HADRONIC ABSORPTION OF COSMIC RAYS WITH BRANCHING

The locality of energy deposition of a CR particle can be justified as follows. Suppose, in a hadronic interaction, a fraction f of the energy in a baryon beam is retained while the rest of the energy is deposited into the target medium. The effective path-length for energy deposition in the presence of branching is then

$$\bar{r}_{p\pi} = \frac{\sum_{k=1} k\, r_{p\pi}\, W_k(f)}{\sum_{k=1} W_k(f)} \tag{B1}$$

where $r_{p\pi}$ is the interaction mean-free path for the dominant interaction (i.e. pp). Here, the energy weighting factor is $W_k = f^{k-1}(1 - f)$, and it is normalized, i.e.

$$\sum_{k=1} W_k(f) = 1 . \tag{B2}$$

It follows that

$$\bar{r}_{p\pi} = r_{p\pi}(1 - f) + 2 r_{p\pi} f(1 - f)$$
$$\qquad + 3 r_{p\pi} f^2 (1 - f) + 4 r_{p\pi} f^3 (1 - f) + \cdots$$
$$= r_{p\pi}(1 - f) \left(\frac{d}{df} \sum_{k=1} f^k \right)$$
$$= r_{p\pi} (1 - f)^{-1} . \tag{B3}$$

The elasticity (i.e. energy that is retained by hadrons after an interaction) of the pp interaction is around $f = 0.3$. By equation (B3), this gives the effective interaction mean-free path as $10 r_{p\pi}/7$. For containment of the charged CR particles within the galaxy, $r_{p\pi}/c \ll t_{con}$, the particle containment time scale. Hence, the approximation of total energy transfer to secondary pions at the first point of hadronic interaction is justified.

This paper has been typeset from a TEX/LATEX file prepared by the author.